Chapter 9

Plates and Shells

Section 9.1 deals with shallow shells and plates with initial imperfection. The mathematical model is derived, and governing PDEs are reduced to ODEs. Reliability of the obtained numerical results is studied. Chaotic vibrations of spherical and conical shells with constant and variable thicknesses have been examined.

In particular, the spatio-temporal chaotic dynamics and control of chaos have been analyzed. Vibrations of flexible axially-symmetric shells are studied in Section 9.2. The mathematical model has been derived, and supplemented with boundary and initial conditions. The FDM and computational algorithm are presented. The method of relaxation has been described and then applied to study the shell vibrations.

Problems devoted to dynamical stability loss including stability criteria, and scenarios of transition from periodic to chaotic vibrations are analyzed. Then, the shell vibrations under non-uniform harmonic excitation are studied including discussion regarding the existence of Sharkovsky's periodicity series. Control of shell chaotic vibrations using the continuous harmonic local force and the harmonic torque is addressed.

Then, the wavelet-based analysis of chaotic shell vibrations is presented. Numerous novel chaotic phenomena are detected and studied.

9.1 Plates with Initial Imperfections

9.1.1 *Mathematical model and solutions algorithm*

In this chapter, we consider a shallow elastic shell (Fig. 9.1), which can be treated as a plate with initial imperfection (this will be discussed later), located in a closed 3D space of R^3 with curvilinear system of coordinates $\alpha,\ \beta, \gamma$ [Kantor (1971)]. We assume that Lamé parameters A, B and radii R_1', R_{12}, R_2' of the shell mean surface are continuous with their first derivatives regarding the functions α, β.

In the given coordinates, the shell as a part of the 3D space is defined as follows: $\Omega = \{\alpha, \beta, \gamma/(\alpha, \beta, \gamma) \in [0, a] \times [0, b] \times [-{}^{h}/_{2}, {}^{h}/_{2}]\}$. The derived PDEs governing nonlinear dynamics of shells (Fig. 9.1) are obtained on the basis of the following hypotheses: shell fibres are one-layer, made of an isotropic, homogeneous and elastic material, and the Kirchhoff–Love hypothesis holds.

The associated variational equation has the following form [Kantor (1971)]:

$$\delta \iint_{\bar{S}} \left\{ \frac{D}{2} \left[(\Delta \bar{w})^2 - (1-\nu) L(\bar{w}, \bar{w}) \right] - \left[\Delta_k \bar{F} + L\left(\frac{1}{2}\bar{w} + \bar{w}_0, \bar{F} \right) \right] \bar{w} \right.$$

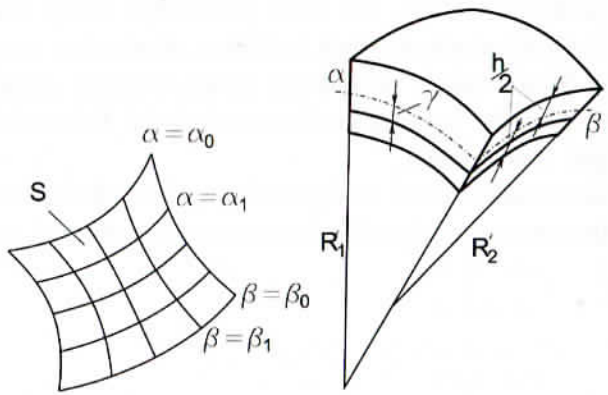

Fig. 9.1 Computational scheme of a shallow shell.

$$\left. - \frac{1}{2Eh} \left[(\Delta \bar{F})^2 - (1+\nu) L(\bar{F}, \bar{F}) \right] \right\} ds$$

$$- \iint_{\bar{S}} \left[q - \frac{h}{\gamma g} (\ddot{\bar{w}} + \varepsilon \dot{\bar{w}}) \right] \delta \bar{w} d\bar{s} = 0. \qquad (9.1)$$

where

$$\Delta = \frac{1}{AB} \left(\frac{\partial}{\partial \bar{\alpha}} \frac{B}{A} \frac{\partial}{\partial \bar{\alpha}} + \frac{\partial}{\partial \bar{\beta}} \frac{A}{B} \frac{\partial}{\partial \bar{\beta}} \right),$$

$$\Delta_k = \frac{1}{AB} \left(\frac{\partial}{\partial \bar{\alpha}} \frac{1}{R_1'} \frac{B}{A} \frac{\partial}{\partial \bar{\alpha}} + \frac{\partial}{\partial \bar{\alpha}} \frac{1}{R_{12}} \frac{\partial}{\partial \bar{\beta}} + \frac{\partial}{\partial \bar{\beta}} \frac{1}{R_{12}} \frac{\partial}{\partial \bar{\alpha}} + \frac{\partial}{\partial \bar{\beta}} \frac{1}{R_1'} \frac{A}{B} \frac{\partial}{\partial \bar{\beta}} \right),$$

$$L(\bar{w}, \bar{F}) = \frac{\partial^2 \bar{w}}{\partial \bar{\alpha}^2} \cdot \frac{\partial^2 \bar{F}}{\partial \bar{\beta}^2} - 2 \frac{\partial^2 \bar{w}}{\partial \bar{\alpha} \partial \bar{\beta}} \cdot \frac{\partial \bar{F}^2}{\partial \bar{\alpha} \partial \bar{\beta}} + \frac{\partial^2 \bar{w}}{\partial \bar{\beta}^2} \cdot \frac{\partial^2 \bar{F}}{\partial \bar{\alpha}^2}.$$

In order to solve Eq. (9.1), in which the deflection function $\bar{w}$ and stress function $\bar{F}$ are independently variated, we cannot apply the Ritz procedure directly (equation does not have the form of functional variation being equal to zero). In order to find the approximated value of elements $\bar{w}$ and $\bar{F}$, we take the coordinate sequence $w_i(\alpha, \beta)$ and $\varphi_i(\alpha, \beta)$, satisfying the same requirements as Eq. (9.1).

In order to find $\bar{w}$ and $\bar{F}$, the systems of functions $\{\varphi_{ij}(x, y), \psi_{ij}(x, y)\}$, $i, j = 0, 1, 2 \ldots$, should satisfy the following five requirements:

1. $\varphi_{ij}(x, y) \in H_A$, $\psi_{ij}(x, y) \in H_A$, where H_A is a Hilbert space, which is called the energetic space;
2. $\forall i, j$ functions $\varphi_{ij}(x, y)$ and $\psi_{ij}(x, y)$ are linearly independent, continuous with their partial derivatives to fourth-order inclusively in the space Ω;
3. $\varphi_{ij}(x, y)$ and $\psi_{ij}(x, y)$ satisfy the boundary conditions;
4. $\varphi_{ij}(x, y)$ and $\psi_{ij}(x, y)$ are compact in H_A;

5. $\varphi_{ij}(x,y)$ and $\psi_{ij}(x,y)$ should represent M first elements of the full system of the functions:

$$\bar{w} = \sum_{i=0}^{M_x} \bar{x}_i(\bar{t}) w_i(\bar{\alpha},\bar{\beta}), \quad \bar{F} = \sum_{i=0}^{M_x} \bar{y}_i(\bar{t}) \varphi_i(\bar{\alpha},\bar{\beta}). \tag{9.2}$$

The approximating solutions have coefficients $\bar{x}_i(\bar{t})$ and $\bar{y}_i(\bar{t})$, which are time-dependent functions. Substituting relations (9.2) into Eq. (9.1), carrying out the variational operation, and comparing to zero terms standing by $\delta\bar{x}_i$, $\delta\bar{y}_i$, we get the following system of ODEs for $\bar{x}_i(\bar{t})$ and $\bar{y}_i(\bar{t})$:

$$\begin{gathered} K_{ik}(\ddot{x}_k + \varepsilon\dot{x}_k) + B_{ik}x_k + C_{ip}y_p + D_{ikp}x_k y_p = Q_i q_0, \\ C_{pi}x_i + E_{pj}y_j + \frac{1}{2}D_{pki}x_k x_i = 0, \\ i,\ k = 1,\ 2,\ \ldots,\ n; \quad p,\ j = 1,\ 2,\ \ldots,\ m. \end{gathered} \tag{9.3}$$

In the polar coordinates with axial symmetry $w = w(r)$, $\varphi = \varphi(r)$, $\alpha = r$, $\beta = \theta$, $ds = 2\pi r dr$, and the operators take the form

$$\Delta = \frac{d^2}{d\bar{r}^2} + \frac{1}{\bar{r}}\frac{d}{dr}, \quad L(\bar{w},\bar{F}) = \frac{d^2\bar{w}}{d\bar{r}^2}\cdot\frac{1}{\bar{r}}\frac{d\bar{F}}{d\bar{r}} + \frac{1}{r}\frac{d\bar{w}}{d\bar{r}}\cdot\frac{d^2\bar{F}}{d\bar{r}^2}. \tag{9.4}$$

Substituting $\bar{r}$ by $a\bar{\rho}$ in operators (9.4), and carrying out the standard transformations (and after division by $2\pi E h_0^5/a^4$), the system is transformed to its counterpart non-dimensional form. In order to reduce Eq. (9.3) to the non-dimensional forms, the following quantities are introduced: $\bar{w} = w/h$, $\bar{x}_i = x_i/h$, $\bar{\varphi} = \frac{\varphi}{Eh^3}$, $y_i = \frac{\bar{y}_i}{Eh^3}$, $h = \frac{h(\rho)}{h}$, $h = h(0)$, $\bar{F} = Eh^2F$, $\bar{t} = t\tau$, $\bar{\varepsilon} = \varepsilon/\tau$, $\tau = \frac{a}{h_0}\sqrt{\frac{a^2\gamma}{Eg}}$, $\bar{q} = q\frac{Eh_0^4}{a^4}$, where w is the deflection, F is the stress function, t is time, ε is the damping coefficient, a is the dimension of the square shell, respectively; h is the thickness of the shell, g is the Earth acceleration, γ is the material weight density, ν is Poisson's coefficient for the isotropic material ($\nu = 0.3$), E is elasticity modulus, w_0 is the initial imperfection. Next, bars over the non-dimensional quantities are omitted.

In the case of axially symmetric deformation of the shallow rotation shell of thickness $h = h_0(1 + c\rho)$, the coefficients of system (9.3) take the following form

$$\begin{gathered} K_{ik} = \int_0^1 (1 + c\rho)\, w_i w_k \rho d\rho, \\ N_{ik} = \frac{1}{12(1-\nu^2)}\int_0^1 (1+c\rho)^3 \left[\Delta w_i \Delta w_k - (1-\nu)\, L(w_i, w_k)\right] \rho d\rho, \\ C_{ip} = -\int_0^1 \left[\Delta_k \phi_p + L(w_0, \phi_p)\right] w_i \rho d\rho, \\ D_{ikp} = -\int_0^1 w_i L(w_k, w_p)\rho d\rho, \qquad Q_i = \int_0^1 w_i \rho d\rho, \\ E_{jp} = -\int_0^1 \frac{1}{1+c\rho}\left[\Delta\varphi_j \Delta\varphi_p - (1+\nu)\, L(\varphi_j, \varphi_p)\right]\rho d\rho. \end{gathered} \tag{9.5}$$

Solving the second equation of system (9.3) for y_i, we get

$$y_i = \left[E_{jp}^{-1}C_{ps} + \frac{1}{2}\left(E_{jp}^{-1}D_{pi}x_i\right)_s\right] x_s. \tag{9.6}$$

Multiplying by K^{-1} the first equation of (9.3) and using notation $\dot{x}_i = r_i$, the problem is reduced to the first-order ODEs of the form

$$\begin{gathered} \dot{r}_i = -\bar{\varepsilon}\, r_i + \left[K_{ik}^{-1}C_{ij} + \left(A_{ik}^{-1}D_{ks}x_s\right)_j\right]\cdot y_j \\ -K_{ik}^{-1}B_{ks}x_s + q_0(\bar{t}\,)K_{ik}^{-1}Q_k, \\ \dot{x}_i = r_i, \\ i,\ k,s = 1,\ 2,\ \ldots,\ n; \quad p,\ j = 1,\ 2,\ \ldots,\ m. \end{gathered} \tag{9.7}$$

The so far introduced transformation has been possible since matrices K_{ik}^{-1} and E_{jp}^{-1} exist if the coordinate functions are linearly independent. Equations (9.7) with the initial conditions $x_i = 0$, $\dot{x}_i = 0$ for $t = 0$, have been solved with the fourth-order Runge–Kutta method.

We consider further the axially symmetric deformation of closed shallow rotational shells and circled plates subjected to uniformly distributed load being normal to the mean shell surface. In polar coordinates and in the case of axial symmetry we have: $w = w(\rho)$,

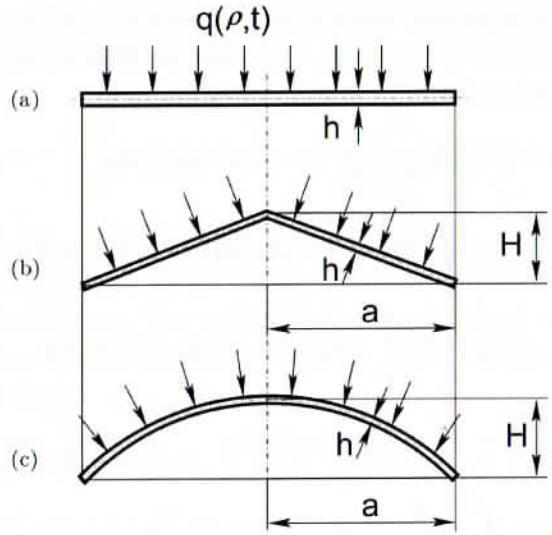

Fig. 9.2 Surfaces of structural members: (a) plate; (b) cone; (c) sphere.

$F = F(\rho)$, $\alpha = \rho$, $\beta = \theta$, $ds = 2\pi\rho d\rho$, and the thickness is defined by the function $h(\rho) = h_0(1 + c\rho)$. The mean shell surface is defined by the initial deflection $w_0 = -hR\left(1 - c_1\rho - c_2\rho^2\right)$, $K = \frac{H}{h_0}$, where H is the full shell height over a plane (see Fig. 9.2).

For $c_1 = 1$, $c_2 = 0$ we get a conical shell [Fig. 9.2(b)]; $c_1 = 0$, $c_2 = 1$ corresponds to a sphere [Fig. 9.2(c)]; for $k = 0$ we deal with a plate [Fig. 9.2(a)].

Approximating function for four types of boundary conditions are shown in Table 9.1. In order to investigate vibrations of a shallow conical shell, we consider it as a plate ($\Delta_k\varphi \equiv 0$) with initial deflection: $w_0 = -k(1 - \tilde{\rho})$, $k = {}^{H}/_{h_o}$, and we apply the coordinate functions given in Table 9.1. Each of the formulas of (9.5) can be presented by a sum of integrals of the following form

$$I(x, y) = \int_0^1 \rho^x (1 - \rho^2)^y d\rho = \frac{(2y)!!(x-1)!!}{(x + 2y + 1)!!}, \qquad (9.8)$$

and for four types of the boundary conditions applied, the coefficients of the system (9.7) take the form:

Table 9.1 System of approximating functions for boundary conditions.

$\psi_j(\rho)$	$\varphi_i(\rho)$	
	$(1-\rho^2)^{i+1}$	$(1-\rho^2)^i$
ρ^{2j}	movable clamping 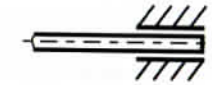	fixed simple support 
$(1-\rho^2)^{j+1}$	fixed clamping 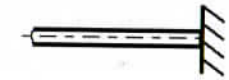	movable simple support 

1. Unmovable clamping

$$K_{ik}^{(1)} = \frac{1}{6 + 2i + 2k} + c\frac{(4 + 2i + 2k)!!}{(7 + 2i + 2k)!!},$$

$$N_{ik}^{(1)} = \frac{4(i+1)(k+1)}{3(1-\nu^2)}\left\{\frac{1}{i+k+1}\left\{\frac{ik}{(i+k)(i+k+1)}\right.\right.$$
$$\left. + \frac{3c^2}{2(i+k+2)}\left[\frac{6ik}{(i+k)(i+k-1)} - \frac{1+\nu}{2}\right]\right\}$$
$$\left. + \frac{3c(2i+2k-4)!!}{(2i+2k+3)!!}\left[15ik - (1+\nu)(i+k)(i+k-1)\right]\right\},$$

$$C_{ip}^{(1)} = -2(p+1)$$
$$\cdot\frac{H}{h_0}\left(-\int_0^1 (1-r^2)^{i+p+1}dr + 2p\int_0^1 r^2(1-r^2)^{i+p}dr\right),$$

$$E_{jp}^{(1)} = 4ip\left[(j+p-1)(1+\nu) - 2jp\right]$$
$$\times\left(\frac{1}{j+p-1} - \frac{c}{j+p-{}^1/_2} + \frac{c^2}{j+p}\right),$$

$$D_{ikp}^{(1)} = 4(i+1)(k+1)p\frac{p!}{(i+k+1)\ldots(i+k+p+1)}$$

$$Q_i = \frac{1}{2(i+2)}. \qquad (9.9)$$

2. Movable clamping

$$K_{ik}^{(2)} = K_{ik}^{(1)}, \qquad N_{ik}^{(2)} = N_{ik}^{(1)},$$

$$C_{ip}^{(2)} = 2\frac{H}{h_0} \cdot p(2p-1) \cdot \int_0^1 r^{2p-2} \cdot (1-r^2)^{i+1} dr \qquad Q_i^{(2)} = Q_i^{(1)},$$

$$E_{jp}^{(2)} = -16\,(j+1)\,(p+1) \left\{ \frac{pj}{(j+p+1)\,(j+p)\,(j+p-1)} \right.$$
$$+ \frac{c^2}{2\,(j+p+1)\,(j+p+2)} \left[\frac{6jp}{(j+p)\,(j+p-1)} - \frac{1-\nu}{2} \right]$$
$$\left. - c\frac{(2j+2p-4)!!}{(2j+2p+3)!!} \left[15jp - (1-\nu)\,(j+p)\,(j+p-1) \right] \right\},$$

$$D_{ikp}^{(2)} = -\frac{4\,(i+1)\,(k+1)\,(p+1)}{(i+k+p+1)\,(i+k+p+2)}. \tag{9.10}$$

3. Unmovable simple support

$$K_{ik}^{(3)} = K_{i-1,k-1}^{(1)}$$

$$N_{ik}^{(3)} = \begin{cases} \dfrac{2+c\,(4+3c)}{6\,(1-\nu)}, & k=i=1, \\ -\dfrac{c\,(4+5c)}{15\,(1-\nu)}, & i=1,\ k=2;\ i=2,\ k=1, \\ N_{i-1,k-1}^{(1)}, \end{cases}$$

$$C_{ip}^{(3)} = C_{i-1,p}^{(1)}, \quad D_{ikp}^{(3)} = D_{i-1,k-1,p}^{(1)}, \quad Q_i^{(3)} = Q_{i-1}^{(1)}, \quad E_{jp}^{(3)} = E_{jp}^{(1)}. \tag{9.11}$$

4. Movable simple support

$$\begin{aligned} &K_{ik}^{(4)} = K_{i-1,k-1}^{(1)}, \quad N_{ik}^{(4)} = N_{ik}^{(3)}, \quad C_{ip}^{(4)} = C_{i-1,p}^{(2)}, \\ &D_{ikp}^{(4)} = D_{i-1,k-1,p}^{(2)}, \quad Q_i^{(4)} = Q_{i-1}^{(1)}, \quad E_{jp}^{(4)} = E_{jp}^{(2)}. \end{aligned} \tag{9.12}$$

As it has been already mentioned, once we investigate the spherical shell we treat it as a plate with the initial deflection $w_0 = -k(1-r^2)$. For four types of boundary conditions shown in Table

9.1, the coefficients (9.7) differ from the case of the conical shell only by C_{ip}:

1. Unmovable clamping: $C_{ip}^{(1)} = -4\frac{H}{h_0} p \frac{(1+i)!\,p!}{(i+p+1)!}$.
2. Movable clamping: $C_{ip}^{(2)} = 4\frac{H}{h_0}\,(i+1)\,(p+1)\,\frac{(i+p)!}{(i+p+2)!}$.
3. Unmovable simple support: $C_{ip}^{(3)} = C_{i-1,p}^{(1)}$.
4. Movable simple support: $C_{ip}^{(4)} = C_{i-1,p}^{(2)}$.

The transversal uniformly distributed harmonic load is $q = q_0 \sin(\omega_p t)$, where q_0 is the amplitude of the harmonic excitation and ω_p is a frequency of the excitation.

9.1.2 *Results reliability*

In order to study PDEs governing dynamics of the mentioned structural members, we introduce mode shape functions and obtain ODEs of infinite dimension. In order to get correct interpretation of the obtained results, the following remarks should be taken into account. When we investigate any continuous system, instead of infinite set of ODEs, we take a truncated system of finite dimension. It is assumed that by increasing a number of equations, we find a threshold beginning from which a further increase in the number of equations does not yield anything new in the system behaviour. This approach is also motivated by an occurrence of finite dimension of the system attractor. However, it may happen that an improper choice of basis functions, which serve to reduce PDEs to ODEs, effects the corresponding system of ODEs, which may have attractors different from that of the original system.

This feature may occur, for instance, in the case of a 2D equation governing dynamics of heat convection. The Lorenz system [Lorenz (1963)], presenting a three-mode truncation of the derived approximated PDE, demonstrated complex dynamics including chaos. However, an increase in the number of modes yields first an irregular increase in chaos, and hence its decrease. For sufficiently large number of modes, chaos vanishes. In the work [Curry *et al.* (1984)] it has been shown that for large Prandtl numbers δ in the considered 2D

Boissinesque convection there are critical values of the Rayleigh number Ra implying two- and three-mode vibrational motion, whereas with further increase in Ra, the system exhibits a periodic one-frequency convection. The illustrated example shows that in order to get qualitatively true correspondence between the original and truncated dynamics obtained by the use of either Bubnov–Galerkin or Ritz approaches, we need to take into account a sufficient number of modes. Let us investigate the problem of estimating the number of modes in the Ritz procedure using an example of vibrations of spherical and conical shallow shells being geometrically nonlinear and having a constant or non-constant thickness, and being bounded by their contour. The applied load (uniformly distributed along the shell surface) has the following form

$$q = q_0 \sin(\omega_p t). \tag{9.13}$$

We consider the vibration charts associated with shells of $k = 3$ and $k = 5$ (Figs. 9.3 and 9.4, respectively) depending on the magnitude of control parameters $\{q_0, \omega_p\}$ for different number of

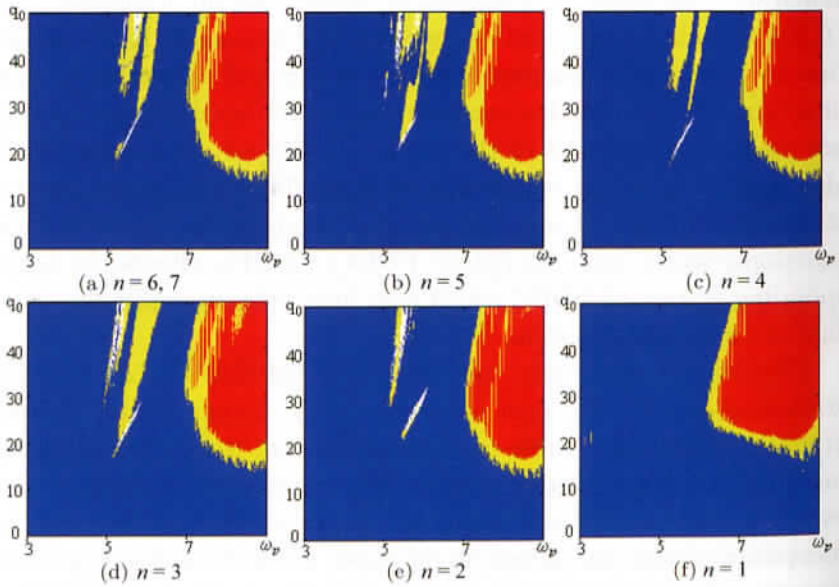

Fig. 9.3 Charts of control parameters $\{q_0, \omega_p\}$ of the conical shell for $k = 3$ and for different n.

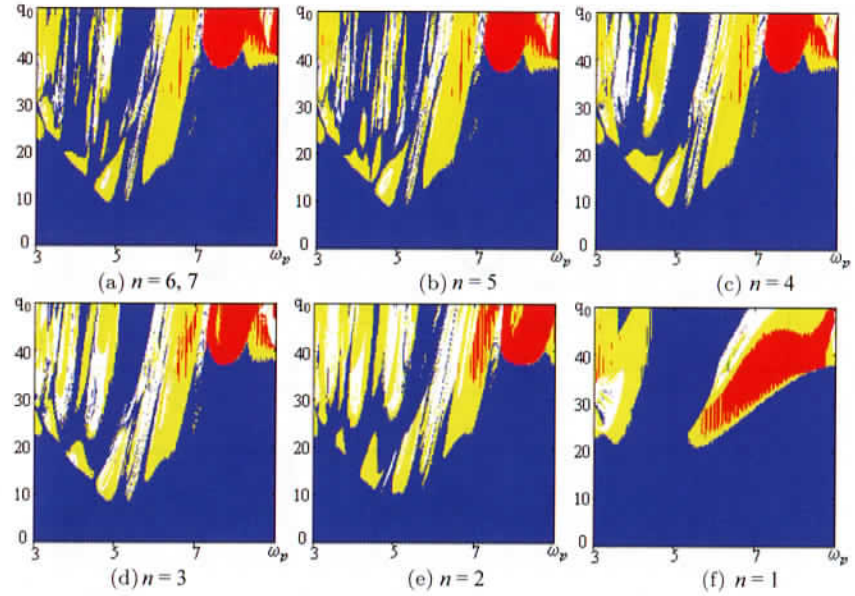

Fig. 9.4 Charts of control parameters $\{q_0, \omega_p\}$ of the conical shell for $k = 5$ and for different n.

partition terms $n = 1 - 7$. Further increase in the number n in (9.3) has not changed the charts $\{q_0, \omega_p\}$ qualitatively. For $n = 1$ (Fig. 9.3), the chart differs from the remaining ones, i.e. it presents only bifurcation zones and harmonic and sub-harmonic vibrations with ω_p and $\omega_p/2$, without any chaotic zones. Increasing n yields new zones of bifurcation and chaos.

Similarly, the chart ($k = 5$) for $n = 1$ strongly differs from the remaining ones, since an increase in n yields different zones becoming similar, i.e. the converging sequence of vibration character is observed. For instance, the sub-harmonic zone is the same for all $n \geq 2$, but for $n = 2$ it is shifted to the right. Chaotic zones become smaller while increasing n, but the separated parts do not change starting from $n = 4$. Both cases of $k = 5$ and $k = 3$ exhibit better convergence for high frequencies than low frequencies, and for frequencies located in the neighborhood of the natural frequency.

We consider two points: the first one for $k = 3$, $n = 6, 7$ is located in a bifurcation zone (Fig. 9.5); the second one, for $k = 5$, $n = 6, 7$ is

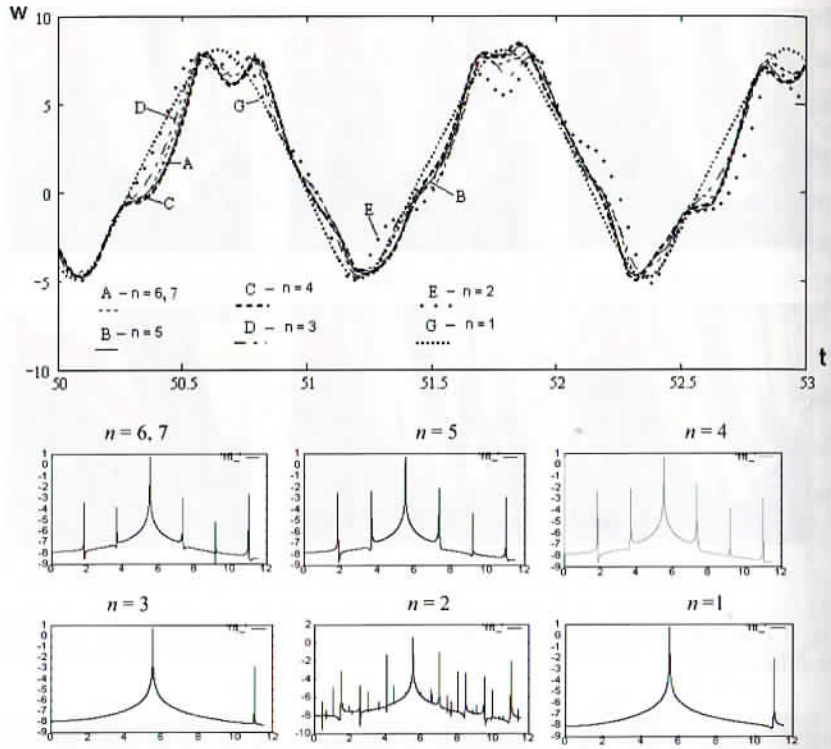

Fig. 9.5 Dependence $w(0,t)$, $t \in [50;53]$ and $S(\omega)$ versus n for the conical shell ($k = 3$) with constant thickness (movable clamping).

in a chaotic zone (Fig. 9.6). In Fig. 9.5, $w\,(0,t)$ for $50 \leq t \leq 53$ and power spectra ($S(\omega)$) are reported. Analysis of the given results in Fig. 9.5 shows that beginning from $n \geq 4$ dependences $w(0.5 : t)$ are close to each other, whereas power spectra coincide in full.

Results obtained for $n = 1, 2, 3$ differ essentially from those of $n \geq 4$. Hence, we may conclude that beginning from $n \geq 4$, the process of bifurcations is reliable for $k \leq 3$, i.e. there exists a convergent sequence, which can be modelled in the following way

$$\left[w^0 - \sum_{i=1}^{n} x_i(t) w_i(\rho)\right] = \min_{t\in[50,53]}, \quad \left[\varphi^0 - \sum_{i=1}^{n} y_i(t) w_i(\rho)\right] = \min_{t\in[50,53]}, \tag{9.14}$$

and this is the best approximation to w^0 and φ^0 in the metric H_A.

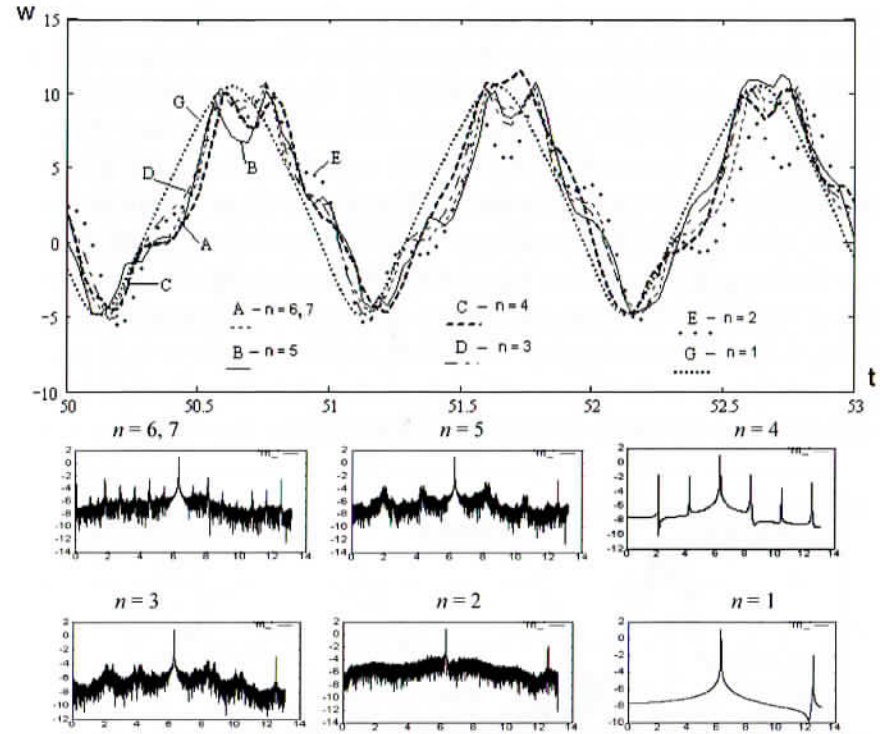

Fig. 9.6 Dependence $w(0,t)$, $t \in [50;53]$ and $S(\omega)$ versus n for the conical shell ($k = 5$) with constant thickness (movable clamping).

For $n = 4, 5, 6, 7$, the power spectrum exhibits a period tripling bifurcation, and the attracting orbits have period-3. Occurrence of period-3 orbits yields the occurrence of orbits with periods $n = 1, 2, 3 \ldots$. The mentioned remarks are applicable to both real functions and maps of an interval into itself. Here, we aim at an analysis of other orbits, which are exhibited by dynamics of the flexible conical shells. In Fig. 9.6, the same characteristics as in Fig. 9.5 are shown. However, in this case we do not observe the previously exhibited uniform convergence.

For $n = 1$, we have periodic vibrations; $n = 4$ corresponds to the period tripling bifurcation (period-3), where period-1 is defined by $2\pi/\omega$; for $n = 2, 3, 5, 6, 7$ though we have determined chaotic vibrations, we deal with different types of chaos. Namely, for $n = 2$

we have chaos associated with excitation frequency. For $n = 3, 5$ we have chaos exhibiting mainly frequency 3ω, whereas for $n = 6, 7$ we have chaos associated with frequency 7ω. Owing to this discussion, we may conclude that a convergence of the Ritz procedure versus a number of the terms of the series (9.3) essentially depends on initial deflection parameter k, and on the dynamical regime of the system.

In what follows, we investigate convergence of the Ritz procedure versus boundary condition type and a shell geometry using an example of conical shells supported along their edges and having constant (Fig. 9.7) and non-constant (Fig. 9.8) thicknesses ($h = h_0(1 + c\rho)$) for $c = 0.1$, $k = 5$. We consider a point, which for $n = 6, 7$ is in a chaotic zone for the following fixed parameters: $q_0 = 2.4$, $\omega_p = 3.5$.

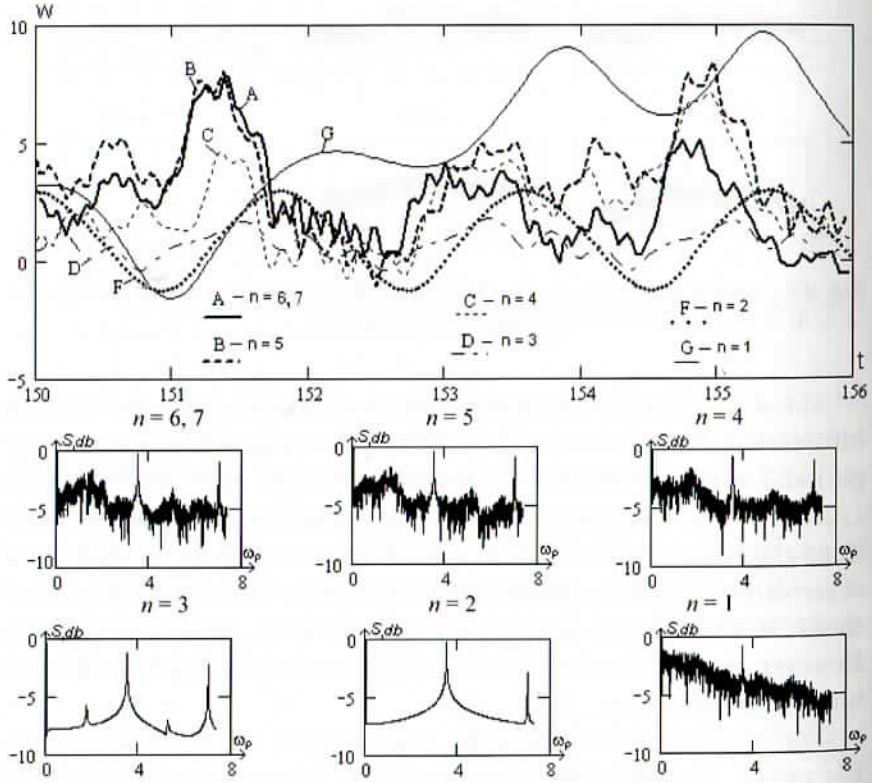

Fig. 9.7 Dependence $w(0, t)$, $t \in [50; 53]$ and $S(\omega)$ versus n for the conical shell ($k = 5$) with constant thickness (movable simple clamping).

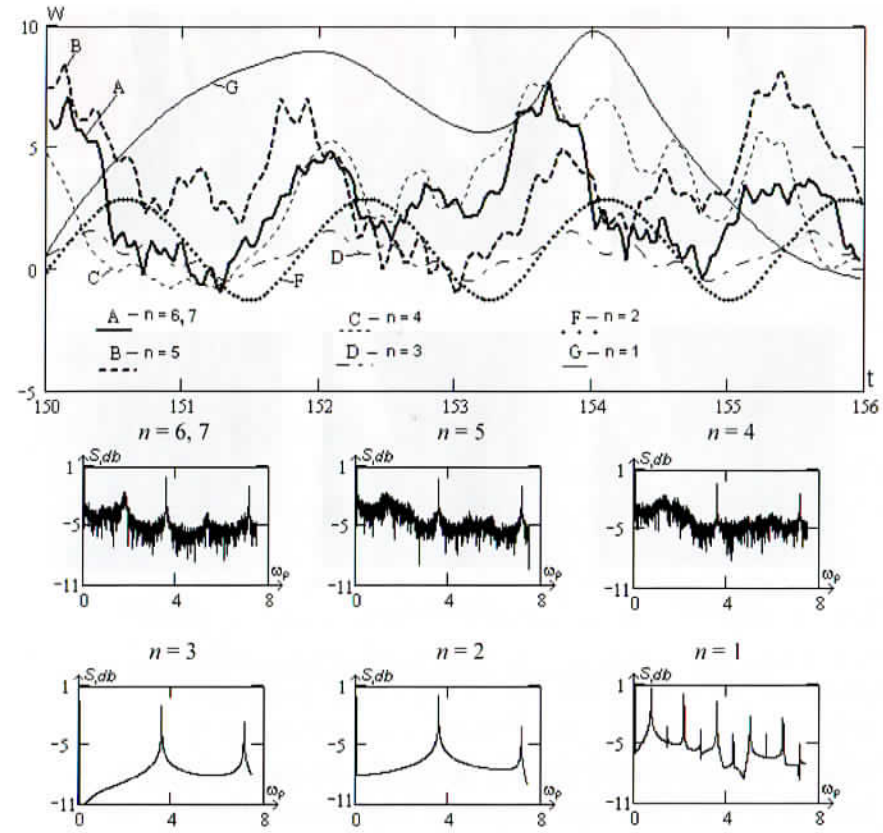

Fig. 9.8 Dependence $w(0, t)$, $t \in [50; 53]$ and $S(\omega)$ versus n for the conical shell ($k = 5$) with the non-constant thickness (movable simple clamping).

In Fig. 9.7, signals ($w(0; t)$, $150 \le t \le 156$) and power spectra are reported. For $n = 2$, harmonic vibrations with ω_p occur, $n = 3$ yields the first period doubling bifurcation, whereas for $n = 1, 4, 5, 6, 7$ we have chaos associated with the fundamental shell frequency.

Next, we consider the shell with variable thickness and with the following fixed parameters: $q_0 = 2.4$, $\omega_p = 3.57$. In Fig. 9.8, signals ($w(0; t)$, $150 \le t \le 156$) and power spectra are reported. For $n = 2$ and $n = 3$, periodic vibrations with the frequency ω_p are shown; $n = 1$ yields sub-harmonic vibrations of $\omega_p/5$, i.e. the first approximation of (9.3) yields period-5 vibration, whereas for $n = 4, 5, 6$ chaos

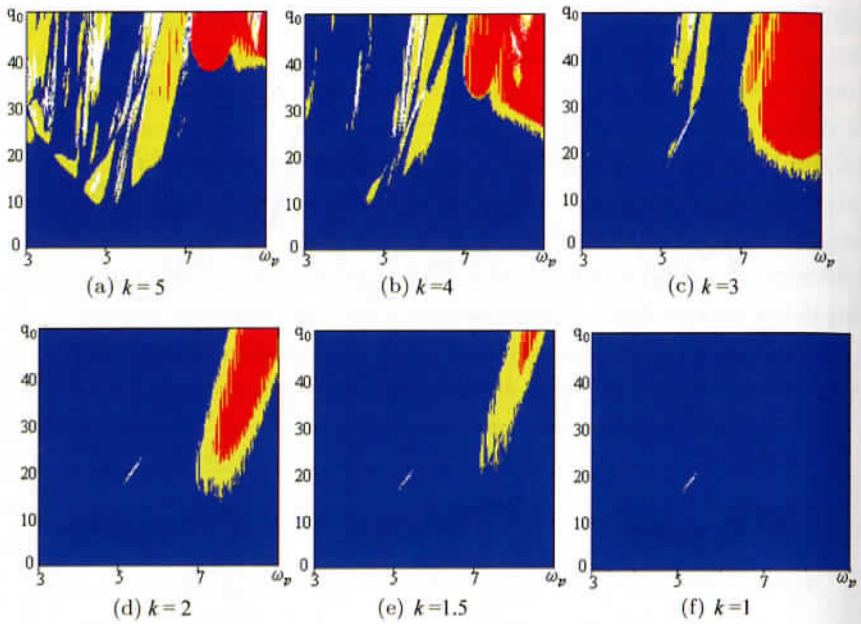

Fig. 9.9 Charts $\{q_0, \omega_p\}$ of the spherical shell for different n.

occurs associated with natural frequency. In other words, beginning from $n = 4$, a convergent sequence is observed. Further, all results are reported for $n = 6$.

9.1.3 *Spherical shells of constant thickness*

We consider vibrations of spherical shallow shells with constant thickness, supported on their edges. In Fig. 9.9, charts of control parameters $\{q_0, \omega_p\}$ for the shell with $k = 1, 1.5, 2, 3, 4, 5$, are reported. The chart showing a transition into chaos exhibits rich dynamics while increasing coefficient k. Analysis of dependence $\{q_0, \omega_p\}$ versus k shows that for the plate ($k = 0$), $\{q_0, \omega_p\}$ exhibits only periodic vibrations under the constraints $w(0) \leq 5$ and $q_0 \leq 100$. Zones of chaos and bifurcations increase with the increase in k, and for $k = 1$ only two chaotic narrow islands within the harmonic zones appear. Increasing $k \geq 1.5$ yields new zones of bifurcation and chaos.

Considering deterministic vibrations of spherical and conical shells with constant and variable thicknesses for arbitrary boundary conditions and k parameter, none of the known models in its pure form can describe a transition to chaos of the studied continuous mechanical systems. The so far mentioned parameters, i.e. q_0, ω_p, k play a key role in the mechanisms of transition of the mechanical system into chaos.

For spherical moveably supported shells a new scenario of transition from periodic to chaotic vibrations has been detected, which exist also in the case of conic shells of both constant and non-constant thickness for the same boundary conditions. There appears a new linearly independent frequency and a transition into chaos is carried out via the series of linear combination of two frequencies and the successive Hopf bifurcations. We consider this scenario in detail on an example of a spherical shell with parameter $k = 3$. The fundamental characteristic signal $w(0, t)$, phase portrait $w(\dot{w})$, power spectrum $S(\omega_p)$, Poincaré section $w(w(t + T))$ are reported. In Table 9.2, the following notation is used: $w_i = w(t)$, $w_{i+1} = w(t + T)$, where T is the period of excitation. The reported q_0 values are called threshold values, since in between the mentioned q_0 values, the chart practically does not change. In what follows, we describe the dynamical phenomena reported in Table 9.2.

1. Vibrations are carried out with the frequency of excitation a_1 and they are periodic. Phase portrait presents on invariant set of one-rotational cycle ($q_0 = 15$).
2. Further increase in the parameter q_0 up to $q_0 = 15.92$ implies an occurrence of the independent frequency b_1, i.e. there is two-frequency motion with frequencies a_1 and b_1. Motion is not synchronized, i.e. $\frac{a_1}{b_1} = \frac{m}{n} = 8.859\ldots$ is irrational.
3. Increase in q_0 up to $q_0 = 17$ yields the series of linearly dependent frequencies $b_n = n \cdot b_1$ and $a_n = a_1 - (n-1)\, b_1$, and this process continues up to the moment, when the frequencies a_k and $b_k \in [b_1, a_1]$ start to approach each other. After that, in the spectrum, a third type of the dependent frequency is exhibited: $c_n = x \pm c_2$, $c_2 = a_7 - b_6$, $x_n = a_n,\ b_n$.

Table 9.2 Vibration characteristics for different q_0.

q_0	w(t)	Phase portrait	Power spectrum	Poincaré map
15.0	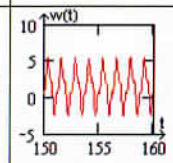	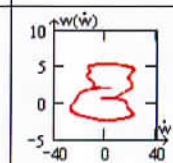	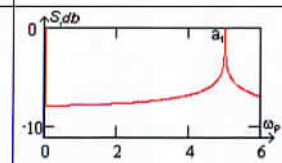	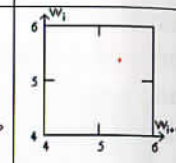
15.92	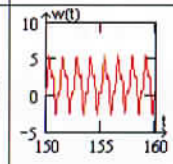	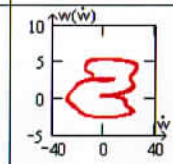	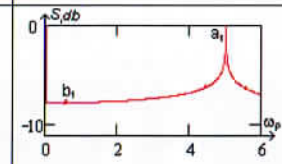	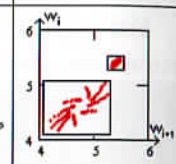
15.95	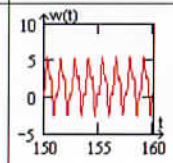	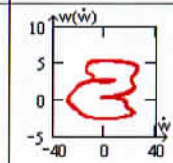	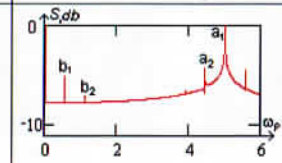	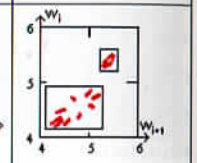
16.0	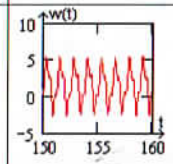	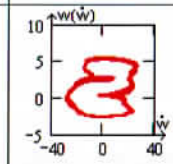	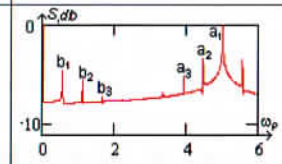	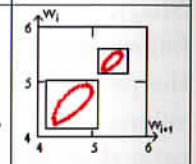
16.3	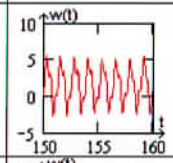	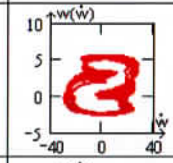	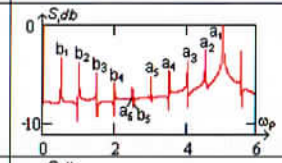	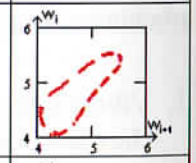
16.7	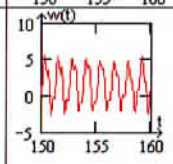	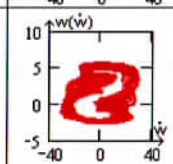	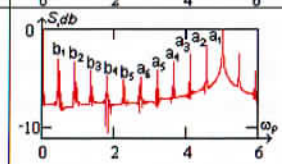	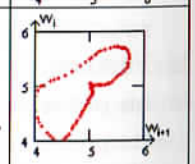
17.0	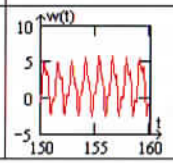	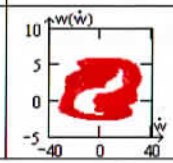	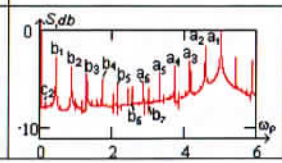	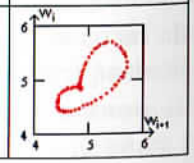

Table 9.2 (*Continued*)

17.35	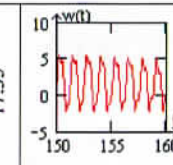	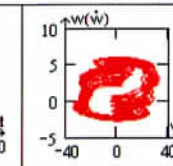	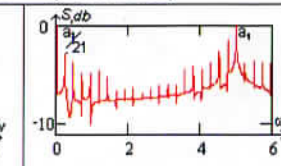	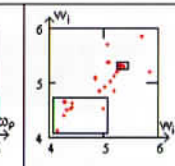
17.382	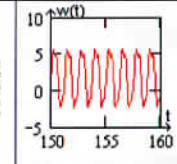	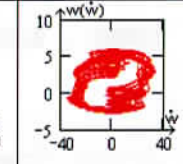	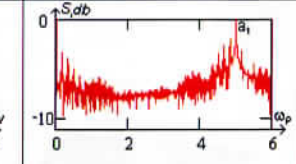	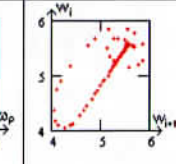
17.383	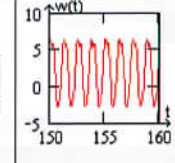	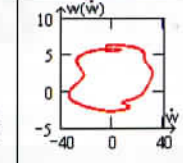	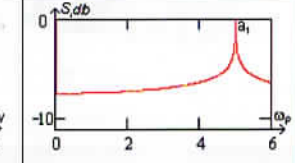	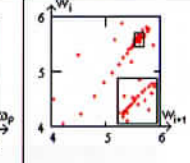

4. Then, we observe mutual approach of further frequencies, and the third type of the dependent frequency vanishes, and period vibrations, with period-21 occurs.
5. For the parameter $q_0 = 16.4$, a period doubling bifurcation for frequency b_1 takes place.
6. Further increase in $q_0 = 17.382$ implies chaos. Change of q_0 on amount of $9 \cdot 10^{-5}$, i.e. for $q_0 = 17.383$, pushes the shell into stiff stability loss (deflections increase suddenly, approximately in two times), and the system again vibrates periodically with the frequency of excitation a_1. Here, we may treat this process as a dynamical stability loss of conical shells subjected to periodic time loading, which can be understood as a novel criterion for the dynamical stability loss. Analysis of the existing dynamical criteria of stability loss of shells is carried out in the reference [Krysko (1976)]. The reported process of the dynamical stability loss is considered as the most general, and its properties before stability loss allow to control the given process.

The spherical shells exhibit narrow zones embeded into chaos, where the Feigenbaum scenario [Feigenbaum (1983)] has been

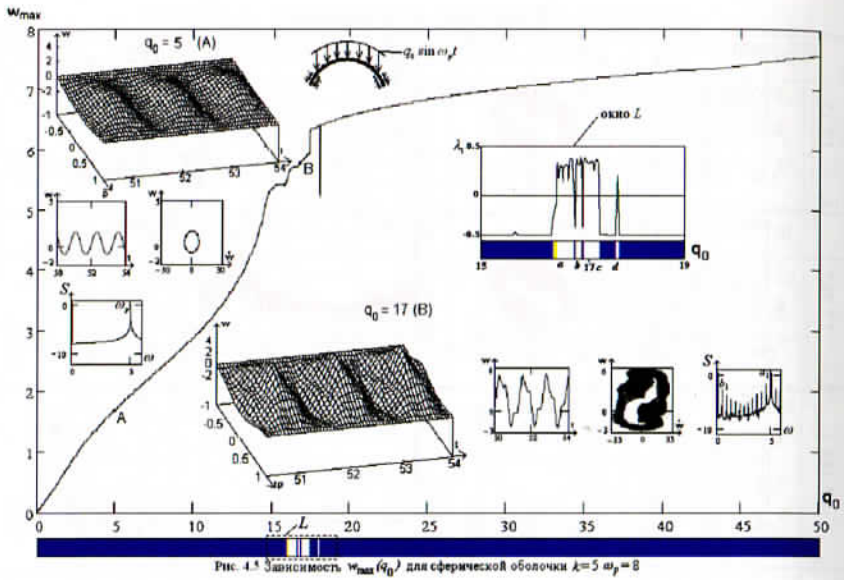

Рис. 4.5 Зависимость $w_{max}(q_0)$ для сферической оболочки $k=5$ $\omega_p=8$

Fig. 9.10 Dependence $w_{\max}(q_0)$ and other dynamical characteristics for the spherical shell ($k = 3$, $\omega_p = 5$).

detected. However, only three period doubling bifurcations have occurred, and further sequence of bifurcations has not been detected numerically.

In order to illustrate vibrations of spherical shells, in Figs. 9.10 and 9.11, the characteristics $w_{\max}$ monitored in the shell top versus q_0 for $\omega_p = 5$, $k = 3$ and for $\omega_p = 8$, $k = 5$ respectively are shown.

The Lyapunov exponents play an important role in investigations of dynamical systems. They give computational qualitative measure of the stochasticity order. The proposed and developed idea of computation of a series of vibration character of dynamical system [Awrejcewicz *et al.* (2002)] based on an analysis of the power spectrum $S(\omega)$ reveals a good coincidence with the evolution of the largest characteristic exponent (LE) named here as $\lambda_1(q_0)$. In this work, in order to compute LE the Benettin method is applied [Bennetin *et al.* (1978, 1979)]. In a chaotic state $\lambda_1 > 0$, and white color corresponds to chaotic zones in the reported scales/charts.

In Fig. 9.10, window L is presented in the form of a scale, for which the dependence $\lambda_1(q_0)$ ($15 \leq q_0 \leq 19$) is shown, and where four zones

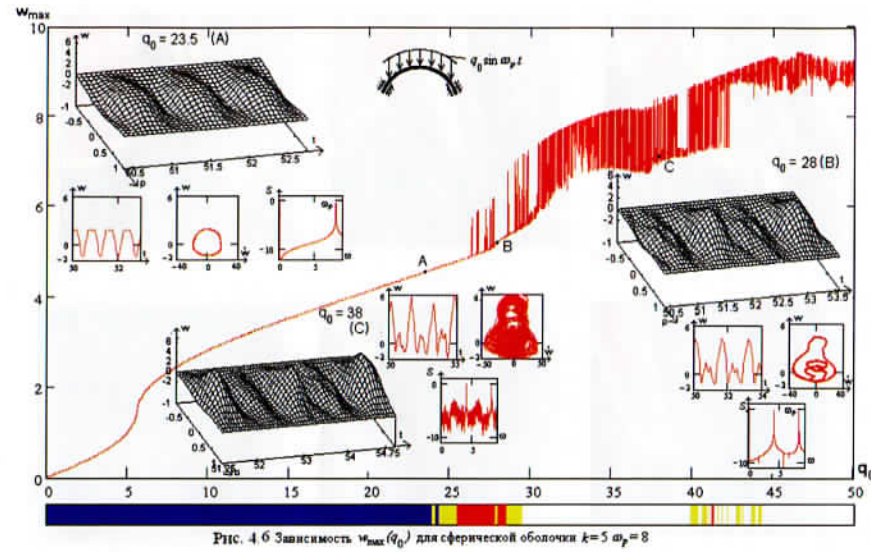

Рис. 4.6 Зависимость $w_{max}(q_0)$ для сферической оболочки $k=5$ $\omega_p=8$

Fig. 9.11 Dependence $w_{\max}(q_0)$ and other dynamical characteristics for the spherical shell ($k = 5$, $\omega_p = 8$).

of chaos are observed: a ($16.1 \leq q_0 \leq 16.5$); b ($16.6 < q_0 < 16.8$); c ($16.9 \leq q_0 \leq 17.3$) and d ($17.9 < q_0 < 18.1$), with $\lambda_1 > 0$, which well coincides with the scale of vibrations. Observe that in zone d, local buckling is observed on the corresponding dependence $w_{\max}(q_0)$. Figures include also $w(t)$, $w(\dot{w})$, power spectra and space forms of vibrations for three points A, B, C for $k = 5$ (point A corresponds to periodic vibrations, point B refers to bifurcations, point C refers to chaos) and two points A, B (point A refers to periodic vibrations, B is the linear combination of two independent frequencies a_1 and b_1 with successive Hopf bifurcations) for $k = 3$, which are shown in dependencies $w_{\max}(q_0)$.

Point A corresponds to harmonic vibrations, point B to linear combination of two independent frequencies, and point C to chaos. Analysis of these results in either two points $w(0, t)$ or in space $w(\rho, t)$ for $50 \leq t \leq 54$ allows to conclude that the dynamical phenomena exhibited by the shell do not depend on k in the case of periodic vibrations, whereas observed bifurcations and chaos essentially depend on parameter k.

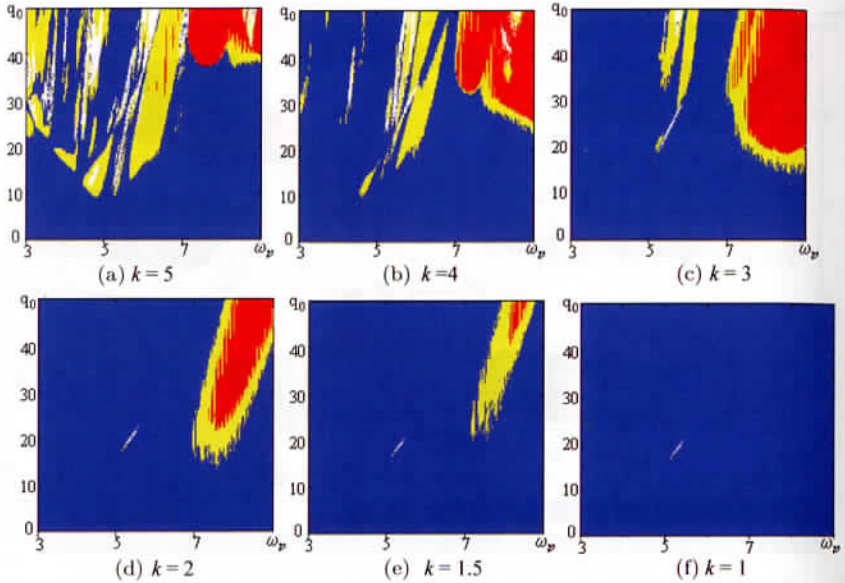

Fig. 9.12 Charts $\{q_0, \omega_p\}$ of the conical shell (movable clamping) for different n.

9.1.4 *Conical shells of constant thickness*

We consider vibrations of conical shallow shells of constant thickness and with the moveable clamping. In Fig. 9.12, the charts $\{q_0, \omega_p\}$ for shells with constant thickness and for $k = 1, 1.5, 2, 3, 4, 5$ are shown. Charts of vibrations character change qualitatively with the increase in k. Let us compare the charts $\{q_0, \omega_p\}$ regarding spherical and conical shells. Analysis of the dependence $\{q_0, \omega_p\}$ versus k shows that an influence of the shell geometry on the character of vibration increases with the increase in k. For $k = 1$, in both conical and spherical shells narrow zones of chaos are located between $\omega_p = 5$ and $\omega_p = 6$. For $k = 1.5$, both charts display bifurcation zones, which are qualitatively similar. For $k = 2$, zones of rational frequencies are added, but they have a different organization. For $k \geq 3$, an influence of the shell geometry implies essential differences in the charts for spherical and conical shells.

Change in the shell geometry has an impact on scenarios of transition into chaos. The conical shell with $k = 5$ exhibits also zones associated with the Feigenbaum scenarios.

In Table 9.3, dependencies of the signal $w(0,t)$, $50 \leq t \leq 60$, the phase portrait $w(\dot{w})$, the power spectrum $S(\omega_p)$ and the Poincaré map $w(w(t+T))$ for the conical shell for $k = 5$ are reported.

Values of the sequence $q_{0,n}$ and the sequence d are given in Table 9.4, which yield the following convergent sequence

$$d_n = \frac{q_{0,n} - q_{0,n-1}}{q_{0,n+1} - q_{0,n}} = 4.66830065.$$

Theoretical value obtained for the function $f = (1 - cx^2)$ is equal to $d = 4.66916224\ldots$. Difference of theoretical computations with the numerical experiments for the conical shell is of 0.018%.

Next, we consider the dependence $w_{\max}(0)$ versus q_0 for $\omega_p = 5.61$ and scales of bifurcations for conical shells $k = 3; 5$, as well as vibrations of the shell's surface in time, signals $w(0,t)$ $51.25 \leq t \leq 53.75$, phase portraits for periodic vibrations, vibrations after the series of bifurcations, and finally chaotic vibrations (Fig. 9.13).

In what follows, we investigate an influence of boundary conditions on the vibrations character with the example of the conical shell with $k = 5$ taking into account boundary conditions of movable clamping and movable simple support (Fig. 9.14). Analysis of the results shows that the vibrations corresponding to the movable clamping are more complex than that of the movable simple support.

In the case of simply supported shells, the interesting phenomenon of signal intermittency has been detected. Table 9.5, gives the signal $w(t)$, the phase portrait $w(\dot{w})$, the power spectrum $S(w)$, the Poincaré map $w(w(t+T))$, where T stands for the excitation period ($\omega_p = 3.5$).

In this scenario, two period doubling bifurcations are obtained, and next the intermittency behavior is observed, which transits the system into chaos.

9.1.5 *Control of chaos*

We investigate the influence of the shell thickness change versus boundary conditions and the shell geometry. We consider shallow conical shells with constant and non-constant thicknesses $h = (1 + c\rho)$, considering them as plates with initial deflection

Table 9.3 Vibrational characteristics of the conical shell ($k = 5$) for different q_0.

q_0	Signal $w(t)$	Phase portrait $w(\dot{w})$	Power spectrum $S(a_p)$	Poincaré map $w(w(t+T))$
9.60584	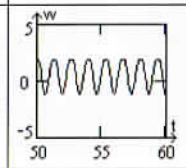	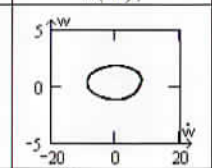	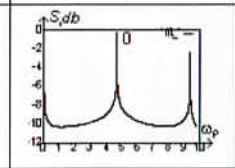	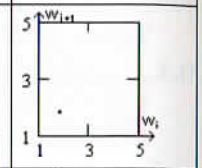
9.60585	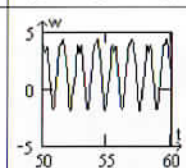	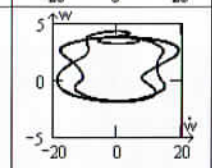	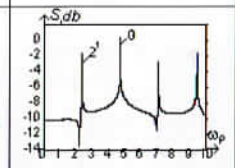	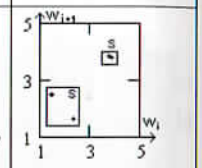
11.098	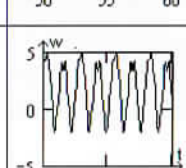	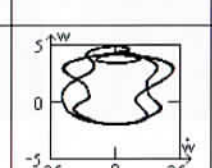	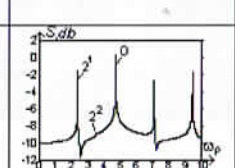	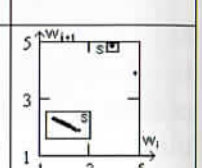
11.7755	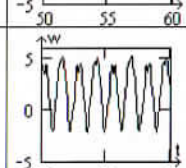	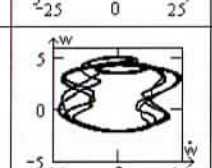	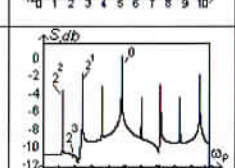	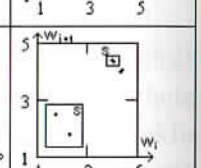
11.9204	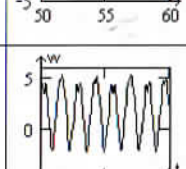	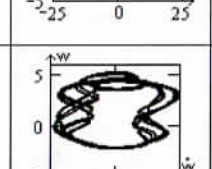	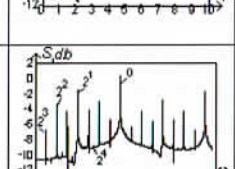	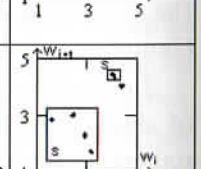
11.951	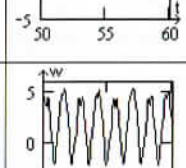	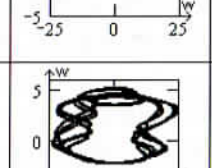	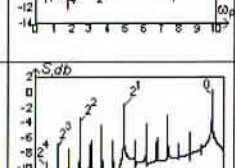	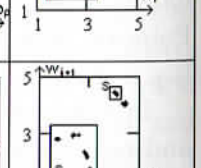
11.97	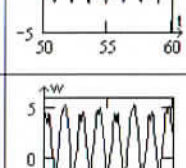	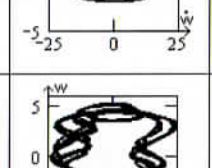	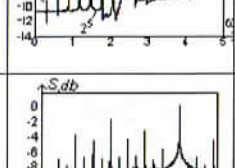	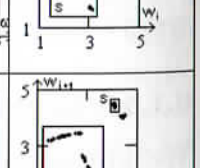

Table 9.4 Feigenbaum scenarios detected numerically.

n	1	2	3	4	5
$q_{0,n}$	9.605846	11.098	11.77755	11.9204	11.951
d_n		2.19579722	4.75708785	4.66830065	

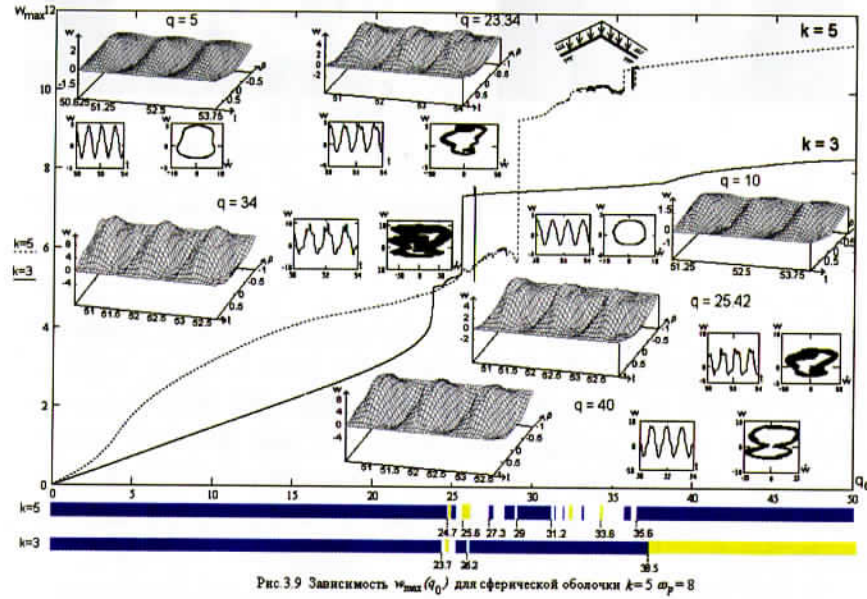

Fig. 9.13 Dependence $w_{\max}(q_0)$ and other dynamical characteristics for the spherical shell ($\omega_p = 8$).

$w_0 = -k(1-\rho)$, where $k = H/h_0$. For the given type of boundary conditions, the approximating functions have the following form

$$w_i(\rho) = (1-\rho^2)^i, \qquad \varphi_j(\rho) = (1-\rho^2)^{i+1}. \tag{9.15}$$

We take the load $q = q_0 \sin \omega_p t$ and zero value initial conditions.

In Fig. 9.15, $\{q_0, \omega_p\}$ charts are reported for constant and non-constant shell thicknesses for $c = 0.1, -0.1, 0.2$ ($k = 5$). Here the influence of thickness changes on the system state differs essentially from the previously studied case.

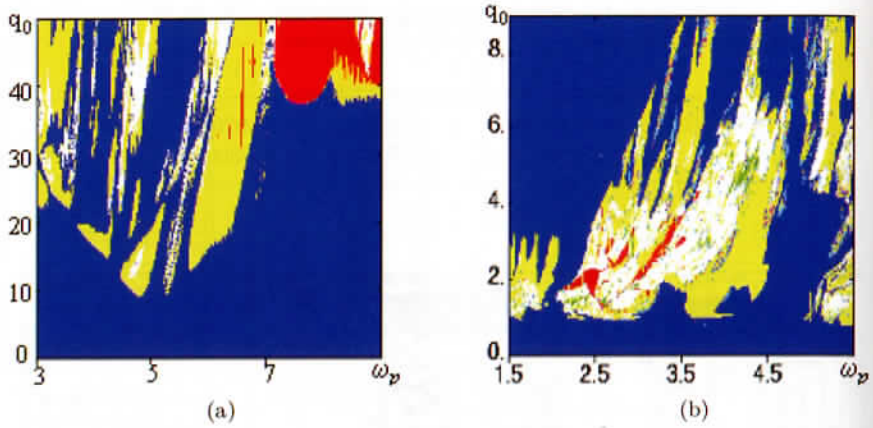

Fig. 9.14 (a) Charts $\{q_0, \omega_p\}$ of the conical shell with movable simple support and (b) with movable clamping.

For $c = -0.1$, a chaotic zone associated with low frequencies (about 2.5) appears, which does not exist for $c = 0.1$, $c = 0.2$ and $c = 0$, as well as a chaotic zone associated with high frequencies (about 5.5) occurs, which exists for $c = 0$ and does not exist for $c = 0.1, 0.2$. It can be seen that the influence of shell thickness change on its dynamics depends essentially on the shell geometry and initial conditions.

In Fig. 9.16, charts of control parameters $\{q_0, \omega_p\}$ for the conical shell ($k = 5$) movably clamped with constant ($c = 0$) and non-constant ($c = 0.1, -0.1$) thicknesses are shown. An increase in thickness in the shell center ($c = -0.1$) yielded new zones of chaos associated with high frequencies and frequencies close to natural frequency for $q_0 > 35$, as well as an increase in zones associated with independent frequencies is observed. For $c = 0.1$, on the contrary, zones of chaos and bifurcations essentially decreased.

In what follows, we analyze spherical shells with $k = 5$. At first, we consider spherical shells with the boundary condition of movable clamping and with $k = 5$ of constant and non-constant thicknesses for $c = 0.1$. In Fig. 9.17, charts of control parameters $\{q_0, \omega_p\}$ are given. Here, the influence of thickness on the shell dynamics is more visible than in the previous case. The charts imply that shells with variable

Table 9.5 The vibration characteristics for the conical shell ($k = 5$) for different q_0.

q_0	Signal $w(t)$	Phase portrait $w(\dot{w})$	Power spectrum $S(a_p)$	Poincaré map $w(w(t-T))$
1.	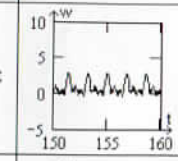	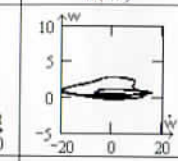	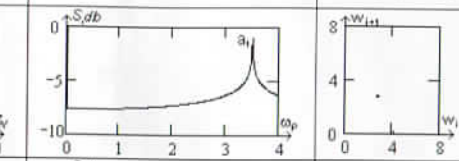	
1.674	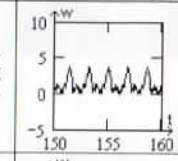	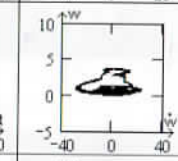	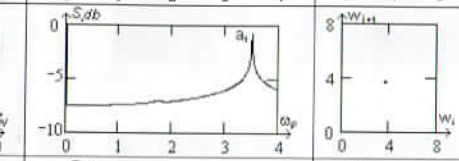	
1.675	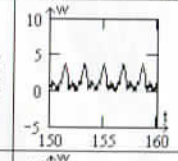	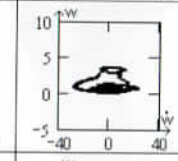	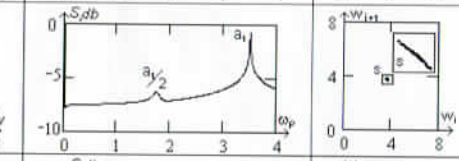	
1.7	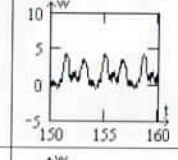	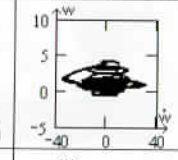	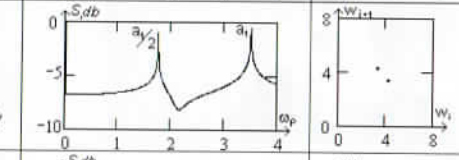	
1.92	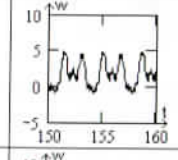	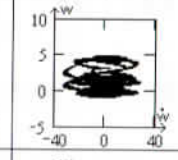	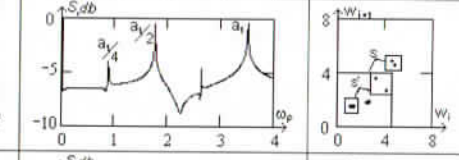	
1.95	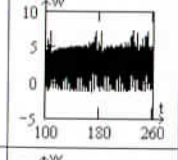	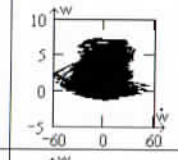	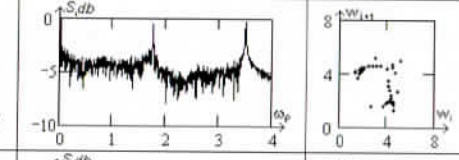	
4.	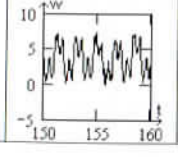	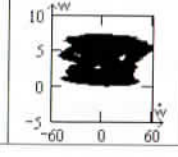	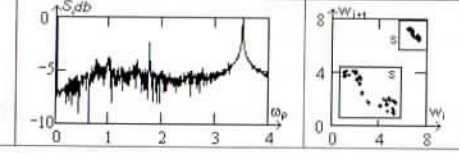	

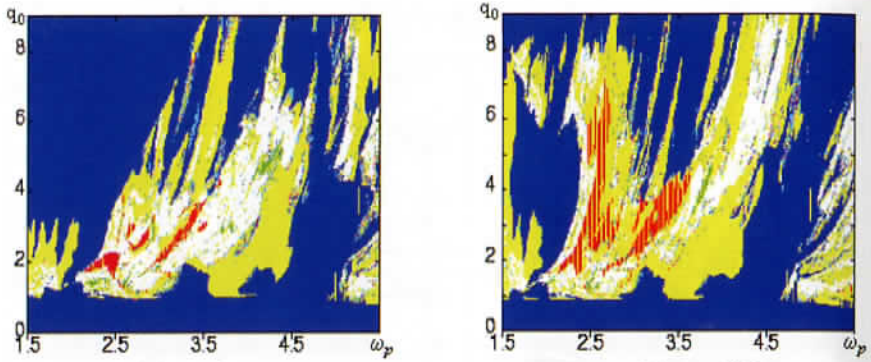

(a) $c = 0$ (b) $c = -0.1$

(c) $c = 0.1$ (d) $c = 0.2$

Fig. 9.15 (a) Charts $\{q_0, \omega_p\}$ for conical shells of constant and (b,c,d) non-constant thickness ($k = 5$).

thickness have smaller zones of bifurcations and chaotic vibrations. The carried out results allow to conclude that by changing the shape of a transversal shell cross-section, and properly choosing parameters q_0 and ω_p we may control nonlinear vibrations of the studied continuous systems.

In order to investigate the vibration character of conical shells versus the parameter q_0 we construct the dependence $w_{\max}(q_0)$. In Fig. 9.18, functions $w_{\max}(q_0)$ in the shell top are given for $k = 5$ and $c = 0,\ 0.1, -0.1$ for $\omega_p = 3.5, 3.57$ and 3.38, respectively. In the dependence $w_{\max}(q_0)$ for $q_0 = 1$, the first stiff stability loss occurs. In the neighborhood of $q_0 = 2$, there is a zone of the second stiff stability loss. Critical loads for constant thickness are within the mentioned

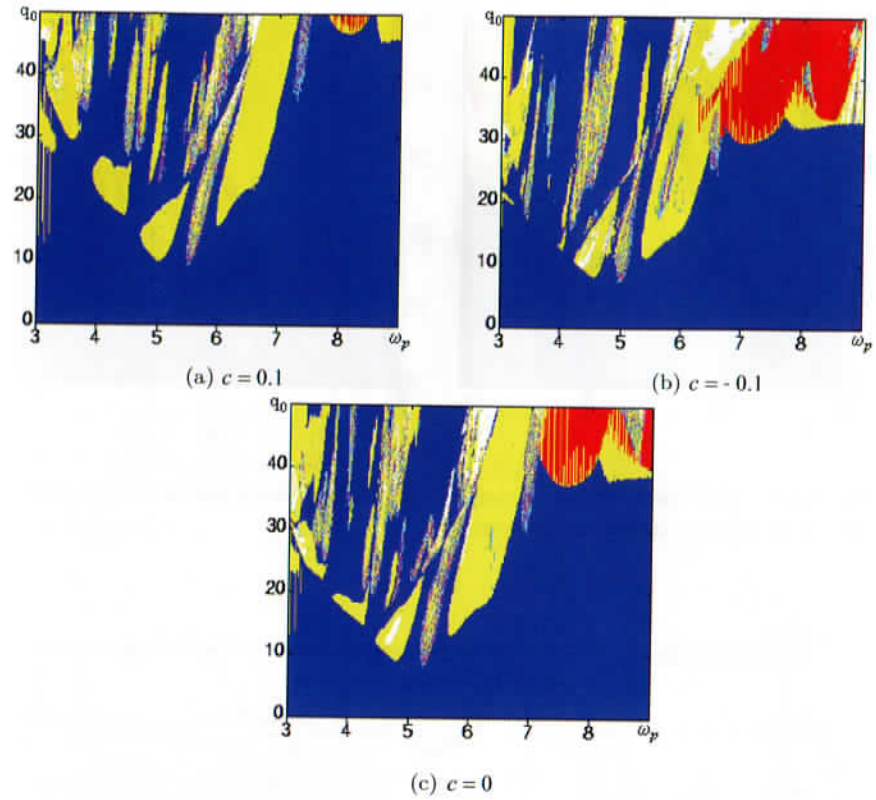

(a) $c = 0.1$ (b) $c = -0.1$

(c) $c = 0$

Fig. 9.16 Charts of control parameters $\{q_0, \omega_p\}$ for spherical shells for different c.

interval. The first critical load occurs for the first Hopf bifurcation ($c = -0.1$) and for the second independent frequency (for $c = 0,\ 0.1$), which are depicted in the scales by vertical lines in the vicinity of $q_0 = 1$.

9.1.6 *Spatio-temporal chaos*

In this section, we investigate the birth of a spatio-temporal chaos in time. In Figs. 9.19 and Fig. 9.20, the signal $w(0, t)$ and the deflection of the mean shell surface in certain time instants for periodic (Fig. 9.19) and chaotic (Fig. 9.20) vibrations for $k = 5$ and $\omega_p = 3.3$ are shown. Besides, there are given dependencies $w(\rho, t)$ for $t \in [151;\ 154.5]$ [Fig. 9.19(a)] and $t \in [167.5;\ 169]$ [Fig. 9.20(a)].

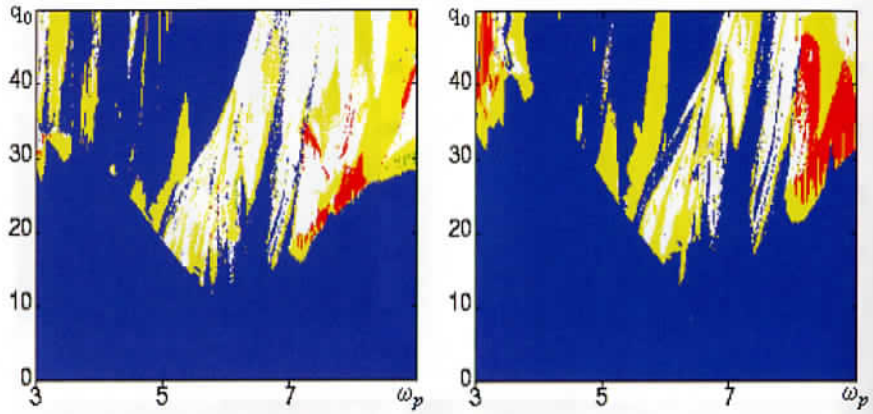

Fig. 9.17 (a) Charts of control parameters $\{q_0, \omega_p\}$ for spherical shells of constant and (b) non-constant thickness ($k = 5$).

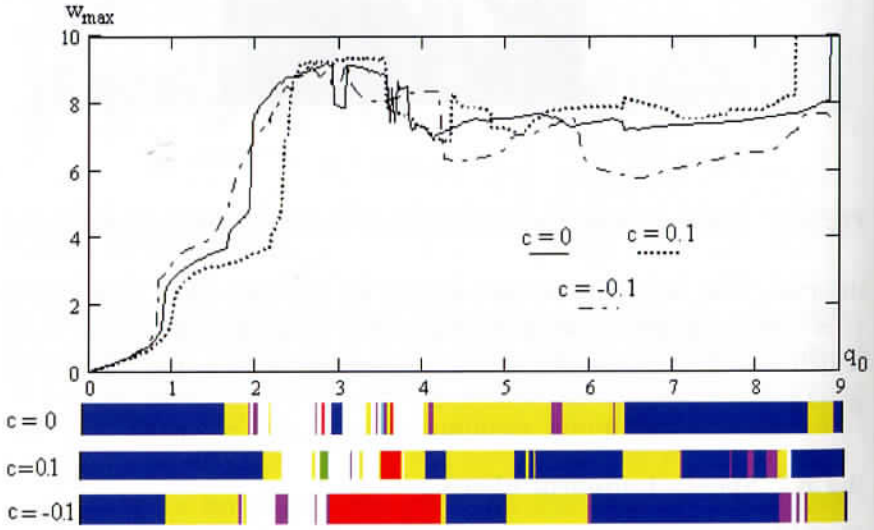

Fig. 9.18 Dependencies $w_{\max}(q_0)$ and vibration scales for different c of the conical shells.

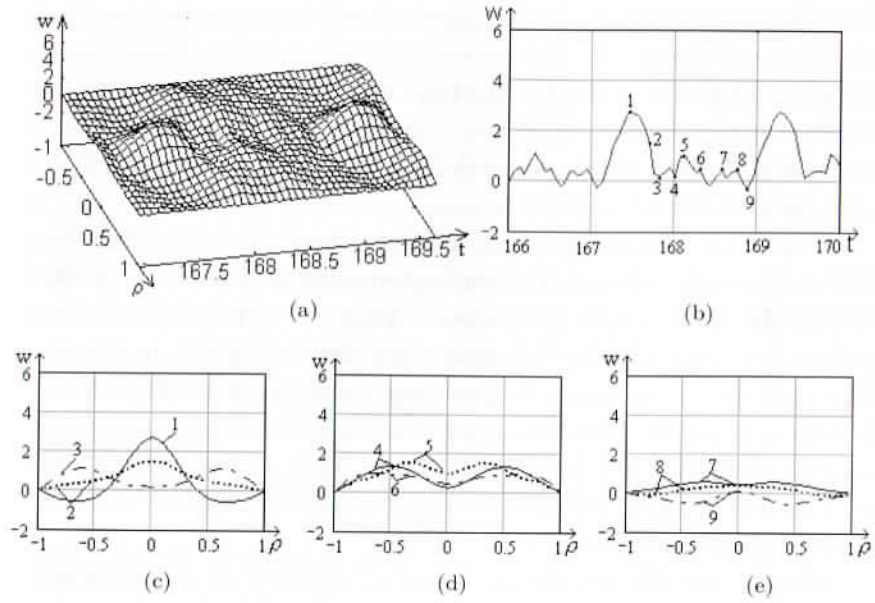

Fig. 9.19 Functions $w(\rho, t)$, $w(t)$ and $w(\rho)$ for periodic regime.

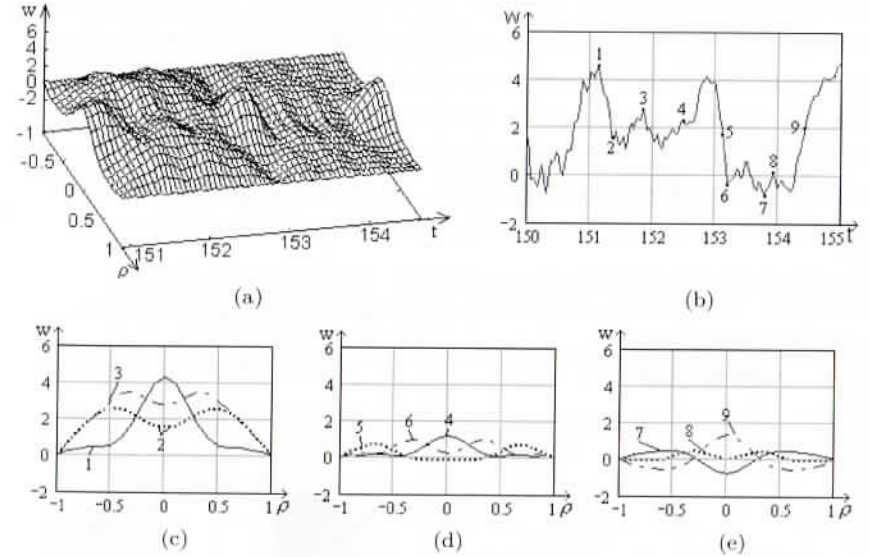

Fig. 9.20 Functions $w(\rho, t)$, $w(t)$ and $w(\rho)$ for chaotic regime.

2. Pinned support of the shell contour
(a) homogeneous BC

$$\frac{\partial \Phi}{\partial r} - \nu \frac{\Phi}{b} = 0, \quad w = 0, \quad \frac{\partial^2 w}{\partial r^2} + \frac{\nu}{r}\frac{\partial w}{\partial r} = 0, \quad \text{for } r = b; \tag{9.19}$$

(b) non-homogeneous BC

$$\frac{\partial \Phi}{\partial r} - \nu \frac{\Phi}{b} = 0, \quad w = 0, \quad \frac{\partial^2 w}{\partial r^2} + \frac{\nu}{r}\frac{\partial w}{\partial r} = M_0 \sin(\omega_p t), \quad \text{for } r = b. \tag{9.20}$$

3. Loosely clamped shell contour

$$\Phi = w = 0, \quad \frac{\partial w}{\partial r} = 0, \quad \text{for } r = b. \tag{9.21}$$

4. Rigidly clamped shell contour

$$\frac{\partial \Phi}{\partial r} - \nu \frac{\Phi}{b} = 0, \quad w = 0, \quad \frac{\partial w}{\partial r} = 0, \quad \text{for } r = b. \tag{9.22}$$

Initial conditions

$$w = f_1(r,\ 0) = 0, \quad w' = f_2(r, 0) = 0, \quad 0 \le t < \infty. \tag{9.23}$$

Top shell conditions

$$\Phi \approx Ar; \quad \Phi' \approx A; \quad w \approx B + Cr^2; \quad w' \approx 2Cr; \quad w'' \approx 2C; \quad w''' \approx 0. \tag{9.24}$$

FDM and computational algorithm

In order to reduce a continuous system (9.16) to a system with lumped parameters, FDM with approximation $O(\Delta^2)$ will be applied. Equation (9.16), in the form of finite-difference relations regarding the spatial coordinate, has the following form

$$w''_i + \varepsilon w'_i = -\frac{w_{i+1} - w_{i-1}}{2\Delta}\left(\frac{1}{r_i^3} - \frac{\Phi_{i+1} - \Phi_{i-1}}{2r_i\Delta}\right) + \frac{w_{i+1} - 2w_i + w_{i-1}}{r_i\Delta^2}\left(\Phi_i + \frac{1}{r_i}\right) - \frac{\Phi_{i+1} - \Phi_{i-1}}{2\Delta} - \frac{\Phi_i}{r_i}$$

$$- \frac{w_{i+2} - 4w_{i+1} + 6w_i - 4w_{i-1} + w_{i-2}}{\Delta^4} - \frac{w_{i+2} - 2w_{i+1} + 2w_{i-1} - w_{i-2}}{r_i\Delta^3} - 4q_i,$$

$$\Phi_{i+1}\left(-\frac{1}{\Delta^2} - \frac{1}{2r_i\Delta}\right) + \Phi_i\left(\frac{2}{\Delta^2} + \frac{1}{r_i^2}\right) + \Phi_{i-1}\left(-\frac{1}{\Delta^2} + \frac{1}{2r_i\Delta}\right) = -\frac{w_{i+1} - w_{i-1}}{2\Delta}\left(1 - \frac{w_{i+1} - w_{i-1}}{4r_i\Delta}\right), \tag{9.25}$$

where $\Delta = b/n$, and n denotes a number of partition of the shell radius. The corresponding boundary conditions are as follows.

1. Simple movable support in a meridian direction
(a) homogeneous BC

$$\Phi = 0, \quad w_{n+1} = -w_{n-1}, \quad w_n = 0 \quad \text{for } r_n = b; \tag{9.26}$$

(b) non-homogeneous BC

$$\Phi = 0, \quad w_{i+1} = M_0 \sin(\omega_p t) - w_{i-1}; \quad w_n = 0, \quad \text{for } r_n = b. \tag{9.27}$$

2. Pinned support of the shell contour
(a) homogeneous BC

$$\Phi_{i+1} = \Phi_{i-1} + \frac{2\Delta\nu}{b}\Phi_i; \quad w_{i+1} = \frac{\nu\Delta - 2b}{2b + \nu\Delta} w_{i-1}; \quad w_n = 0 \quad \text{for } r_n = b; \tag{9.28}$$

(b) non-homogeneous BC

$$\Phi_{i+1} = \Phi_{i-1} + \frac{2\Delta\nu}{b}{}_i; \quad w_{i+1} = \frac{M_0 \sin(\omega_p t) - \left(\frac{1}{\Delta^2} - \frac{\nu}{2b\Delta}\right) w_{i-1}}{\left(\frac{1}{\Delta^2} + \frac{\nu}{2b\Delta}\right)}; \quad w_n = 0 \quad \text{for } r_n = b. \tag{9.29}$$

3. Loosely clamped shell contour

$$\Phi_n = 0; \quad w_{n+1} = w_{n-1}; \quad w_n = 0 \quad \text{for } r_n = b. \tag{9.30}$$

4. Rigidly clamped shell contour

$$\Phi_{i+1} = {}_{i-1} + \frac{2\Delta\nu}{b}{}_i; \quad w_{n+1} = w_{n-1}; \quad w_n = 0 \quad \text{for } r_n = b. \tag{9.31}$$

2. Pinned support of the shell contour
(a) homogeneous BC

$$\frac{\partial \Phi}{\partial r} - \nu \frac{\Phi}{b} = 0, \quad w = 0, \quad \frac{\partial^2 w}{\partial r^2} + \frac{\nu}{r}\frac{\partial w}{\partial r} = 0, \quad \text{for } r = b; \tag{9.19}$$

(b) non-homogeneous BC

$$\frac{\partial \Phi}{\partial r} - \nu \frac{\Phi}{b} = 0, \quad w = 0, \quad \frac{\partial^2 w}{\partial r^2} + \frac{\nu}{r}\frac{\partial w}{\partial r} = M_0 \sin(\omega_p t), \quad \text{for } r = b. \tag{9.20}$$

3. Loosely clamped shell contour

$$\Phi = w = 0, \quad \frac{\partial w}{\partial r} = 0, \quad \text{for } r = b. \tag{9.21}$$

4. Rigidly clamped shell contour

$$\frac{\partial \Phi}{\partial r} - \nu \frac{\Phi}{b} = 0, \quad w = 0, \quad \frac{\partial w}{\partial r} = 0, \quad \text{for } r = b. \tag{9.22}$$

Initial conditions

$$w = f_1(r,\ 0) = 0, \quad w' = f_2(r, 0) = 0, \quad 0 \le t < \infty. \tag{9.23}$$

Top shell conditions

$$\Phi \approx Ar; \quad \Phi' \approx A; \quad w \approx B + Cr^2; \quad w' \approx 2Cr; \quad w'' \approx 2C; \quad w''' \approx 0. \tag{9.24}$$

FDM and computational algorithm

In order to reduce a continuous system (9.16) to a system with lumped parameters, FDM with approximation $O(\Delta^2)$ will be applied. Equation (9.16), in the form of finite-difference relations regarding the spatial coordinate, has the following form

$$w''_i + \varepsilon w'_i = -\frac{w_{i+1} - w_{i-1}}{2\Delta}\left(\frac{1}{r_i^3} - \frac{\Phi_{i+1} - \Phi_{i-1}}{2r_i\Delta}\right) + \frac{w_{i+1} - 2w_i + w_{i-1}}{r_i\Delta^2}\left(\Phi_i + \frac{1}{r_i}\right) - \frac{\Phi_{i+1} - \Phi_{i-1}}{2\Delta} - \frac{\Phi_i}{r_i}$$

$$- \frac{w_{i+2} - 4w_{i+1} + 6w_i - 4w_{i-1} + w_{i-2}}{\Delta^4} - \frac{w_{i+2} - 2w_{i+1} + 2w_{i-1} - w_{i-2}}{r_i\Delta^3} - 4q_i,$$

$$\Phi_{i+1}\left(-\frac{1}{\Delta^2} - \frac{1}{2r_i\Delta}\right) + \Phi_i\left(\frac{2}{\Delta^2} + \frac{1}{r_i^2}\right) + \Phi_{i-1}\left(-\frac{1}{\Delta^2} + \frac{1}{2r_i\Delta}\right) = -\frac{w_{i+1} - w_{i-1}}{2\Delta}\left(1 - \frac{w_{i+1} - w_{i-1}}{4r_i\Delta}\right), \tag{9.25}$$

where $\Delta = b/n$, and n denotes a number of partition of the shell radius. The corresponding boundary conditions are as follows.

1. Simple movable support in a meridian direction
(a) homogeneous BC

$$\Phi = 0, \quad w_{n+1} = -w_{n-1}, \quad w_n = 0 \quad \text{for } r_n = b; \tag{9.26}$$

(b) non-homogeneous BC

$$\Phi = 0, \quad w_{i+1} = M_0 \sin(\omega_p t) - w_{i-1}; \quad w_n = 0, \quad \text{for } r_n = b. \tag{9.27}$$

2. Pinned support of the shell contour
(a) homogeneous BC

$$\Phi_{i+1} = \Phi_{i-1} + \frac{2\Delta\nu}{b}\Phi_i; \quad w_{i+1} = \frac{\nu\Delta - 2b}{2b + \nu\Delta} w_{i-1}; \quad w_n = 0 \quad \text{for } r_n = b; \tag{9.28}$$

(b) non-homogeneous BC

$$\Phi_{i+1} = \Phi_{i-1} + \frac{2\Delta\nu}{b}{}_i; \quad w_{i+1} = \frac{M_0 \sin(\omega_p t) - \left(\frac{1}{\Delta^2} - \frac{\nu}{2b\Delta}\right) w_{i-1}}{\left(\frac{1}{\Delta^2} + \frac{\nu}{2b\Delta}\right)}; \quad w_n = 0 \quad \text{for } r_n = b. \tag{9.29}$$

3. Loosely clamped shell contour

$$\Phi_n = 0; \quad w_{n+1} = w_{n-1}; \quad w_n = 0 \quad \text{for } r_n = b. \tag{9.30}$$

4. Rigidly clamped shell contour

$$\Phi_{i+1} = {}_{i-1} + \frac{2\Delta\nu}{b}{}_i; \quad w_{n+1} = w_{n-1}; \quad w_n = 0 \quad \text{for } r_n = b. \tag{9.31}$$

Initial conditions follow

$$w_n = f_1(r_k, 0) = 0, \quad w'_n = f_2(r_k, 0) = 0,$$
$$(0 \le k \le n), \quad 0 \le t < \infty. \tag{9.32}$$

If we neglect small terms and change the differential operators by the central finite-difference once for $r = \Delta$, the following conditions in the shell top are obtained:

$$\Phi_0 = \Phi_2 - 2\Phi_1; \quad w_0 = \frac{4}{3}w_1 - \frac{1}{3}w_2; \quad w_{-1} = \frac{8}{3}w_1 - \frac{8}{3}w_2 + w_3. \tag{9.33}$$

9.2.2 *Method of relaxation*

The idea of finding a solution to stationary problems via non-stationary problems have been used for the first time in the 1930's of the previous century by A. N. Tichonov [Tichonov and Samarskiy (1977)]. For the problems of stationary supersonic flows acting on the bodies, the relaxation method was applied by Godunov, Zabrodin and Prokhorov in 1961 [Godunov *et al.* (1961)]. In 1947, Lyusternik, in order to solve the Poisson equation using the relaxation method, applied FDM [Lusternik (1947)]. This method has been applied to nonlinear problems of shells by Feodosev [Feodosev (1963)].

In this section, we propose a modification to this method to solve Poisson equation for the Dirichlet problem. In what follows, we illustrate the application of this method with various modifications to nonlinear problems of the theory of circle shallow shells within the Kirchhoff–Love model.

9.2.2.1 *Main Idea*

The main idea of the relaxation method for solutions to numerous problems in mathematical physics relies on the consideration of an unsteady process generated by initial conditions in the limit reaching a steady state, which yields a solution of the associated equilibrium system configurations. The results are obtained fast and in a simpler way than using the method based on direct computation of the equilibrium states. Let us consider the Dirichlet $D = \{0 \le x_1, x_2 \le 1\}$

problem of the Poisson equation on the square defined as follows

$$\frac{\partial^2 u}{\partial {x_1}^2} + \frac{\partial^2 u}{\partial {x_2}^2} = \varphi(x_1, x_2), \quad 0 \le x_1, x_2 \le 1$$
$$u|_{\partial D} = \psi(s), \tag{9.34}$$

having the boundary ∂D, where s is the arc length along the border ∂D, and the functions $\phi(x_1, x_2)$ and $\psi(s)$ are *a priori* given. We formulate the problem (9.34) in the counterpart form

$$\lambda_{x_1 x_2} u_{m n} + \lambda_{x_2 x_2} u_{m n} = \phi\ (x_{1,m}, x_{2,n}), \quad m, n = 1, 2, \ldots, M-1,$$
$$u_{m n}|_{\partial D} = \psi(s_{m n}), \tag{9.35}$$

where $\lambda_{x_1 1}$, $\lambda_{x_2 2}$ are differences of a second-order.

Let us give a physical interpretation of Eq. (9.34). Solution $u(x_1, x_2)$ to the problem (9.34) can be interpreted as a temperature (not dependent on time) in a point (x_1, x_2) of the plate in a heat transfer equilibrium. Functions $\varphi(x_1, x_2)$ and $\psi(s)$ govern the temperature distribution of the heat source in the plate, and the temperature distribution along its border, respectively.

We consider the following supplemented non-stationary problem regarding the heat distribution

$$\frac{\partial U}{\partial t} = \nabla^2 U - \varphi(x_1, x_2),$$
$$U|_{\partial D} = \psi(s); \ U(x_1, x_2, 0) = \psi_0(x_1, x_2), \tag{9.36}$$

where φ and ψ are the same as in problem (9.34), $\psi_0(x_1, x_2)$ is arbitrary given in time instant $t = 0$, i.e. we define the initial conditions, and $\nabla^2(\cdot) = \frac{\partial^2(\cdot)}{\partial x_1^2} + \frac{\partial^2(\cdot)}{\partial x_2^2}$ is the Laplace operator. Since the heat source $\varphi(x_1, x_2)$ and the temperature on the border $\psi(s)$ do not depend on time, we may expect that the solution $U(x_1, x_2, t)$ will be changed more slowly in time. The temperature distribution $U(x_1, x_2, t)$ for $t \to \infty$ tends to the stationary temperature distribution $u(x_1, x_2)$ governed by problem (9.34), i.e. in the case of non-stationary parabolic problems the information can be transmitted only in direction of time increase. Therefore, instead of the stationary problem (9.34) we may solve the associated non-stationary problem (9.36) in time t using the relaxation method until the solution stops

to change in *a priori* given interval of stationary problems. This is the main idea of finding solutions of required accuracy. Owing to this observation, instead of problem (9.34) we solve problem (9.36) and instead of the difference scheme (9.35) we consider and define three different schemes to solve problem (9.36).

We are mainly oriented toward the following simple explicit difference scheme:

$$\frac{1}{\tau}(u^{p+1}_{m\,n} - u^{p}_{m\,n}) = \lambda_{x_1x_1} u^{p}_{m\,n} + \lambda_{x_2x_2} u^{p}_{m\,n} - \varphi(x_{1,m\,n}, x_{2,m\,n}),$$
$$u^{p+1}_{m\,n}\,|_{\partial\,D} = \psi\,(s_{m\,n}), \qquad u^{0}_{m\,n} = \psi_0(x_{1,m} x_{2,\,n}). \tag{9.37}$$

In parallel, we define also the following simple implicit difference scheme

$$\frac{1}{\tau}(u^{p+1}_{m\,n} - u^{p}_{m\,n}) = \lambda_{x_1x_1} u^{p+1}_{m\,n} - \varphi(x_{1,m}, x_{2,n}),$$
$$u^{p+1}_{m\,n}|_{\partial\,D} = \psi(s_{m\,n}), \qquad u^{0}_{m\,n} = \psi_0(x_{1,m}, x_{2,\,n}), \tag{9.38}$$

as well as the following scheme of variable directions

$$\frac{1}{\tau}(\overline{U}_{mn} - U^{0}_{mn}) = \frac{1}{2}\left[\Lambda_{x_1,x_2}\tilde{U}_{mn} + \Lambda_{x_2x_2} U^{p}_{mn} - \varphi(x_{1,m,}x_{2,n})\right],$$
$$\frac{1}{\tau}(U^{p+1}_{mn} - \tilde{U}_{mn}) = \frac{1}{2}\left[\Lambda_{x_1x_1}\tilde{U}_{mn} + \Lambda_{x_2x_2} U^{p+1}_{mn} - \varphi(x_{1,m}x_{2,n})\right],$$
$$U^{p+1}_{mn}\Big|\partial D = \tilde{U}_{mn}\Big|\,\partial D = \Psi(S_{mn}), \quad U^{0}_{mn} = \Psi_0(x_{1,m}, x_{2,n}). \tag{9.39}$$

We assume that $\Psi_0(x_{1,m}, x_{2,n})$ is defined in a way to satisfy the following relation on the border

$$\Psi_0|\,\partial D = \Psi(S_{mn}). \tag{9.40}$$

Computation of $U^{p+1} = \{U^{p+1}_{mn}\}$ on already known $U^{p} = \{U^{p}_{mn}\}$ via the scheme (9.37) is carried out using the explicit formulas. Computation $U^{p+1} = \{U^{p+1}_{mn}\}$ via scheme (9.38) requires solution of the following problem

$$\Lambda_{11} U^{p+1}_{mn} + \Lambda_{x_2x_2} U^{p+1}_{mn} - \frac{1}{\tau} U^{p+1}_{mn} = \varphi(x_{1,m}x_{2,n}) - \frac{1}{\tau} U^{p}_{mn},$$
$$U^{p+1}_{mn}\,|\partial D = \Psi(S_{mn}). \tag{9.41}$$

However, this problem is not simple with respect to the initial problem (9.35). Therefore, there is no rational motivation to apply the implicit scheme to carry out the approximate computation. Finally, computation of $U^{p+1} = \{U^{p+1}_{mn}\}$ based on known $U^{p} = \{U^{p}_{mn}\}$ via scheme (9.39) can be realized in few stages. At first, they are realized in the direction of axis ox_1 to compute solutions $\{\tilde{U}_{mn}\}$ of one-dimensional problems for each fixed n, and then the similar-like computational process is repeated in the direction of axis ox_2 in order to compute solutions $\{U^{p+1}_{mn}\}$ of one-dimensional problems for each fixed m.

A number of arithmetic actions is proportional to a number of unknowns. Consider the difference

$$\varepsilon^{3}_{bm} \equiv U^{p}_{mn} - U_{mn}, \tag{9.42}$$

between the mesh function $U^{p} = \{U^{p}_{mn}\}$ and an exact solution $U = \{U_{mn}\}$ of problem (9.35). Let us compute a condition for which the error ε^{3}_{bm} of solution U^{p}_{mn} of the non-stationary problems tends to zero with the increase in p, as well as the character of this tendency goes to zero. Let us take an optimal step τ and estimate a volume of computational work required to decrease the norm of the initial error

$$\varepsilon^{0}_{bm} = \Psi_0(x_{1,m}, x_{2,n}), \tag{9.43}$$

for a given number of times.

9.2.2.2 *Explicit Scheme of Relaxation*

Solution $\{U_{mn}\}$ of the problem (9.35) satisfies the equations

$$\frac{1}{\tau}(U_{mn} - U_{mn}) = \Lambda_{x_1x_2} U_{mn} + \Lambda_{x_2x_2} U_{mn} - \varphi(x_{1,m}, x_{2,n}),$$
$$U_{mn}\,|\partial D = \Psi(S_{mn}), \qquad U_{mn} = U_{mn1}. \tag{9.44}$$

Taking into account the so far given equations, error ε^{p}_{mn} can be estimated in Eq. (9.37) step by step via the following difference problem, where also Eq. (9.42) is taken into account:

$$\frac{1}{\tau}(\varepsilon^{p+1}_{mn} - \varepsilon^{p}_{mn}) = \Lambda_{x_1x_2}\varepsilon^{p}_{mn} + \Lambda_{x_2x_2}\varepsilon^{p}_{mn},$$
$$\varepsilon^{p+1}_{mn}\,|\partial D = 0, \quad \varepsilon^{0}_{mn} = \Psi_0(x_{1,m}, x_{2,n}) - U_{mn}. \tag{9.45}$$

Observe that the mesh function ε^0_{mn} for each $p_1(p = 0, 1, \ldots,)$ takes zero value on the border. It can be treated as an element of a linear space of functions defined on the mesh $(x_{1,m}, x_{2,n}) = (mh, nh, m, n = 0, 1, \ldots, N)$, and taking zero values in points on ∂D. We define the following norm in this space:

$$\|\varepsilon^p\| = \left(\sum_{mn} |\varepsilon^p_{mn}|^2\right)^{\frac{1}{2}}. \tag{9.46}$$

In order to solve (Eq. 9.45), we apply the following finite Fourier series

$$\varepsilon^p = \sum_{rs} (c_{rs}\lambda^p_{rs})\Psi^{(r,s)}, \tag{9.47}$$

where c_{rs} are the coefficients of the series of initial error $\varepsilon^0 = \{\varepsilon^0_{mn}\}$ of the finite Fourier series, and the numbers λ_{rs} are defined in the following way

$$\lambda_{rs} = 1 - \frac{4\tau}{h^2}\left(\sin^2\frac{r\pi}{2M} + \sin^2\frac{s\pi}{2M}\right). \tag{9.48}$$

Numbers $c^p_{rs} = c_{rs}\lambda^p_{rs}$ are coefficients of the development of error $\varepsilon^p = \{\varepsilon^p_{mx}\}$ into the Fourier series via the orthogonal basis $\Psi^{(rs)}$. Therefore,

$$\|\varepsilon^p\| = \left(\sum |c_{rs}\lambda^p_{rs}|^2\right)^{\frac{1}{2}}, \quad \|\varepsilon^0\| = \left(\sum |c_{rs}|^2\right)^{\frac{1}{2}}. \tag{9.49}$$

Finally, we get

$$\frac{\|\varepsilon^p\|}{\|\varepsilon^o\|} \leq \{\max|\lambda rs|\}^p. \tag{9.50}$$

Note that ε^0 can be given to satisfy the equation $\varepsilon^0 = \Psi^{(r',s')}$, where (r', s') is a chosen pair for which

$$\max_{rs} |\lambda rs| = |\lambda_{r's'}|, \tag{9.51}$$

i.e. $\lim\limits_{p\to\infty} \|\varepsilon^p\| / \|\varepsilon^0\| = 0$, and $\max\limits_{rs} |\lambda_{rs}| =< 1$. Maximum decrease for τ, where $\max\limits_{rs} |\lambda_{rs}| - \min$, is estimated from Eq. (9.48):

$$\lambda_{\text{left}} = 1 - \frac{8\tau}{h^2}\cos^2\frac{\pi}{2M}, \quad \lambda_{\text{right}} = 1 - \frac{8\tau}{h^2}\sin^2\frac{\pi}{2M}. \tag{9.52}$$

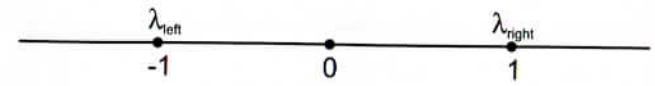

Fig. 9.21 A scheme of τ estimation.

Increasing τ, beginning from $\tau = 0$, we initiate the movement of these points into left (see Fig. 9.21). This process ends when

$$-\lambda_{\text{left}} = \lambda_{\text{right}}. \tag{9.53}$$

Optimal value $\tau = h^2/4$ is yielded by Eq. (9.49):

$$p \geq -\frac{1}{\ln(1 - 2\sin^2\frac{\pi}{2M})} \approx \frac{2M^2}{\pi^2}. \tag{9.54}$$

9.2.2.3 *Method Limits*

The so far described methodology and error estimation are applicable to study difference schemes approximating other boundary value problems for elliptic equations with variable coefficients and with curvilinear boundaries. It is necessary that the operator $-\Lambda_h \equiv -(\Lambda_{x_1x_1} + \Lambda_{x_2x_2})$ occurring in scheme (3.1.2) should be self-jointed, and its eigenvalues μ_j should have the same sign:

$$0 < \mu\min < \mu j < \mu\max. \tag{9.55}$$

9.2.2.4 *Shells with Finite Deflections*

The developed algorithm and programs package allow to solve numerous problems of static and dynamics of axially-symmetric shells. The problems of statics is treated from the point of view of dynamics, and the Feodosev method [Feodosev (1963)] has been applied being a variant of the relaxation method. The method is based on the following approach: for $\varepsilon = \varepsilon_{cr}$ the dependencies $\{q_m,\ w_m(t)\}$ are constructed, where $m = 1, 2, \ldots$ denotes numbers of the load values for which the solution via the mentioned relaxation method has been obtained. This allows for computation of $q(w)$ and analysis of the stress–strain state of shells. We follow here the reference [Valishvili (1976)], where the iterative relaxation method has been illustrated and applied. The functions $q(w)$ constructed via the mentioned algorithm (curves a) and via the method proposed by Valishvili (curves b)

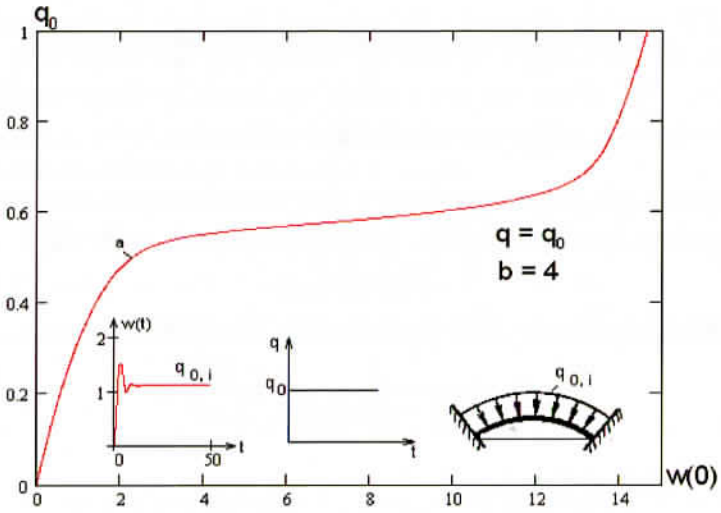

Fig. 9.22 Shell with fixed contour ($q = q_0$, $\varepsilon = 1$).

[Valishvili (1976)] are shown in Figs. 9.22–9.25. Observe that the solution proposed by Valishvili (Fig. 9.23) does not yield either upper or lower critical load values, since both load and deflection are not defined uniquely. On the contrary, the proposed dynamical approach allows to estimate the critical loads accurately, and hence to predict buckling of shells. The occurred loops have the following origin. The given characteristic $q_0(w)$ is constructed for the shell center, whereas the remaining points of the shell radius behave on its own way, i.e. the shell stability loss occurs not in the shell center, but in its quadrants, hence the shell center versus the load describes the mentioned loops. The reported results not only validate the high efficiency of this method, but also authenticate its wide applications to solve problems of statics.

9.2.3 *Dynamical stability loss*

9.2.3.1 *Criterions*

The proposed algorithm and the method of computations allow to investigate the stress–strain states and the stability of the already mentioned wide class of static/dynamic problems of shells. It is well

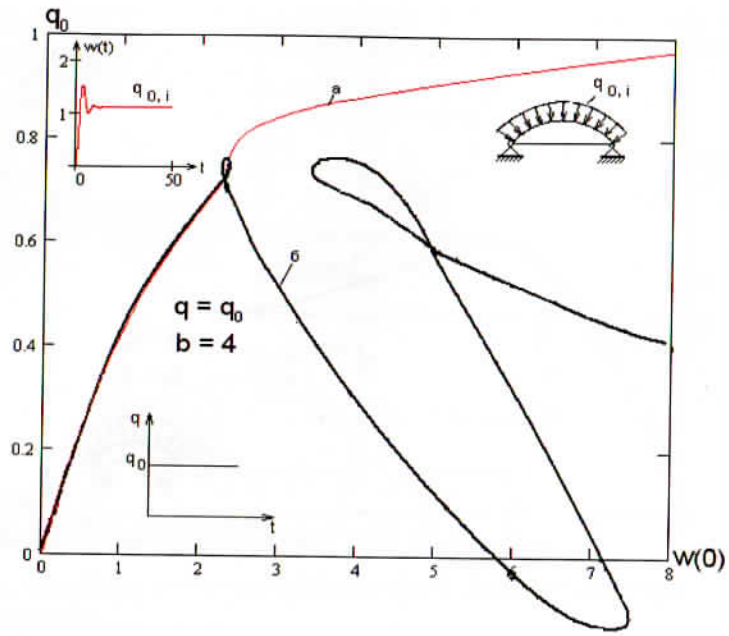

Fig. 9.23 Shell with pinned contour ($q = q_0$, $\varepsilon = 1$).

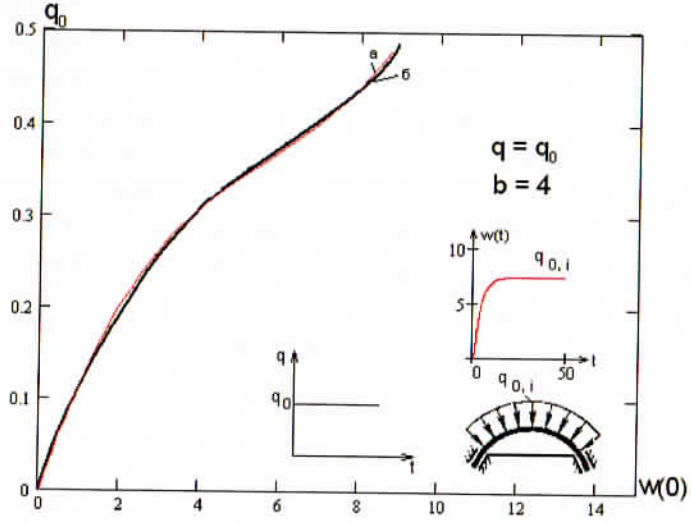

Fig. 9.24 Shell with loosely clamped contour ($q = q_0$, $\varepsilon = 1$).

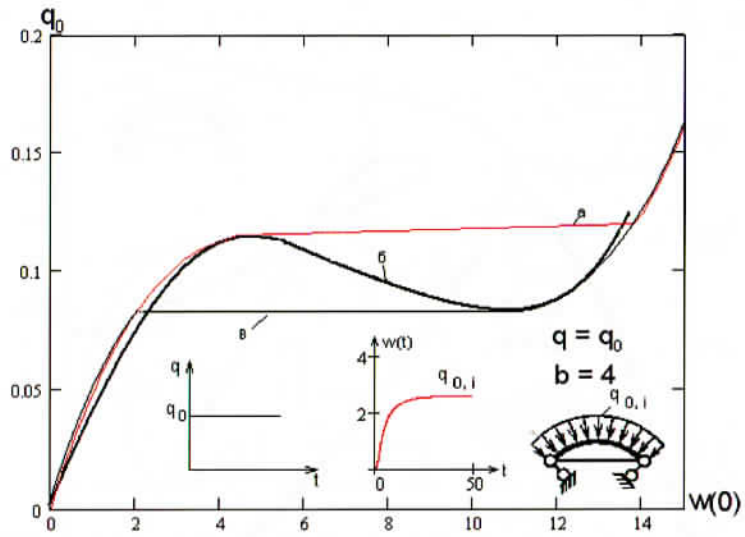

Fig. 9.25 Shell with simple movable contour ($q = q_0,\ \varepsilon = 1$).

known that shell structures subjected to transversal load of different type suffer stability loss. For the dynamical problems of shells we have a series of criteria of dynamical stability loss, and their analysis is carried out in the reference [Krysko (1976)]. We consider shells with parameter $b = 4$ subjected to uniform harmonic transversal load $q = q_0 \sin(\omega_p t)$. In Fig. 9.26, the dependence $w_{\max}(q_0)$ for the shell with a simple-movable contour subjected to the mentioned load action for $\omega_p = 0.521$ is shown. In the mentioned figure, points a, b, c corresponding to periodic, chaotic and post-critical periodic vibration are reported, respectively. Point a — $q_0 = 0.16212$, point b — $q_0 = 0.16213$, i.e. the change of q_0 on magnitude of $1 \cdot 10^{-5}$ implies a sudden increase in shell's deflection (we deal here with a stiff stability loss). The similar-like investigations have been also carried out for the remaining types of the boundary conditions, and the similar results have been obtained in the reference [Krysko (1976)].

While investigating chaotic vibrations, we do not present diagrams about orbits, as it is usually done during investigations of a wide class of two-valued maps into itself, but the vibration scale is constructed instead. Dependence $w_{\max}(q_0)$, scales of vibrations

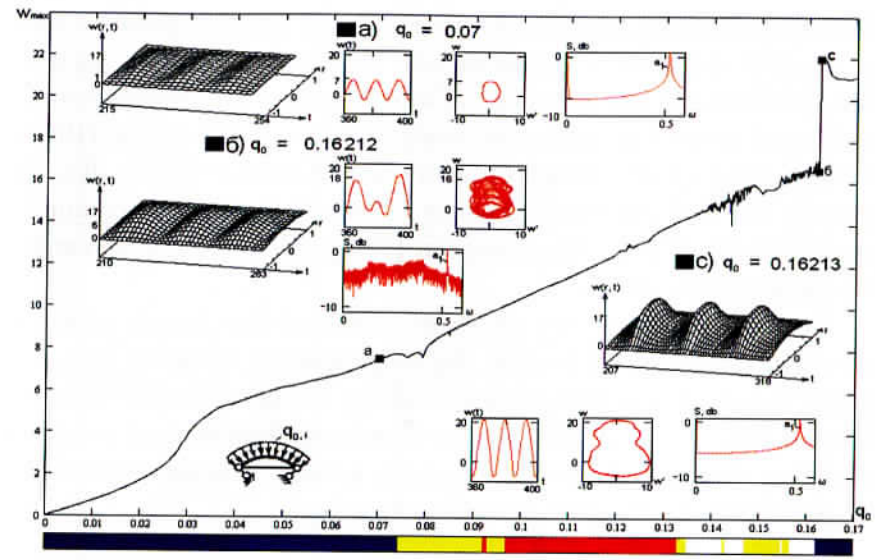

Fig. 9.26 Dependence $w_{\max}(q_0)$ and other dynamic characteristics for the shell with simple movable contour.

character and Lyapunov exponents well coincide with each other approving the validity and reliability of obtained results. When the largest Lyapunov exponent becomes positive, then chaos appears, which is also validated by the scale of bifurcations and $w_{\max}(q_0)$ [Awrejcewicz *et al.* (2006)], where a series of stiff bifurcations is observed (dynamical stability loss). For the given points on the functions $w_{\max}(q_0)$ a surface $w(r,\ t)$, the time history $w(0,\ t)$, the phase portraits $w(w')$ and the power spectrum $S(\omega_p)$ for the shell center are reported (remaining shell points have analogous characteristics). The shell, from its previous chaotic state, is transited into periodic vibrations by a sudden buckling jump. The so far described scenario of stiff stability loss can be understood as the criterion of dynamical stability loss for the case of harmonic transversal excitation. This is a novel criterion of stability loss of shells subjected to periodic loads.

9.2.3.2 *From Periodic to Chaotic Vibrations*

Analysis of nonlinear dynamics of structures plays an important role in the investigation of vibrations of plates and shells periodically

loaded taking into account energy dissipation from the point of view of possible scenarios of transition into chaotic dynamics. In particular, this concerns investigations of axially-symmetric spherical shells subjected to periodic loads and dissipative factors [Agamirov (1990); Goldenveizer *et al.* (1979); Grigoluk and Kabanov (1978); Krysko (2003); Nie and Liu (1994); Palmov (1976); Saliy (2001); Schimmels and Palaiotto (1994); Slawianowska (1996); Soric (1994); Teregulov and Timergalev (1998)].

In problems of theory of shells, some of the known classical scenarios have been detected, like Feigenbaum's scenario, but also their numerous modifications including: modified Ruelle–Takens–Newhouse scenario, Ruelle–Takens–Newhouse–Feigenbaum scenario, modified Pomeau–Manneville scenario, as well as novel scenarios of transition from periodic to chaotic vibrations.

Feigenbaum's scenario

We consider vibration of shells subjected to an action of periodic load $q = q_0 \sin(\omega_p t)$ uniformly distributed on their surfaces. We study possible scenarios of transition of those mechanical systems from periodic to chaotic vibrations, and we briefly discuss a few hypotheses regarding the mechanisms of transition of the regular/laminar flow to the hydro-dynamic turbulence. In spite of the earlier proposed Landau hypothesis [Landau (1944)], all other mechanisms are associated with models of finite dimensions including the Ruelle–Takens–Newhouse, Feigenbaum and Pomeau–Manneville scenarios. It should be mentioned that even now there is no general and unique mechanism of transition into turbulence. We here illustrate and describe mechanisms of occurrence of weak turbulence exhibited by transversal vibrations of flexible axially symmetric shells. Transition from regular to chaotic vibrations via period doubling bifurcations is well known and validated by many simple mathematical models. It is also known that period doubling bifurcations are well described in the Rössler attractor and many other simple models. The mentioned phenomenon has been also detected in our problem of the shell with a simple moveable contour. In Figure 9.27 for the central shell point, and for the boundary condition (Fig. 9.26) the

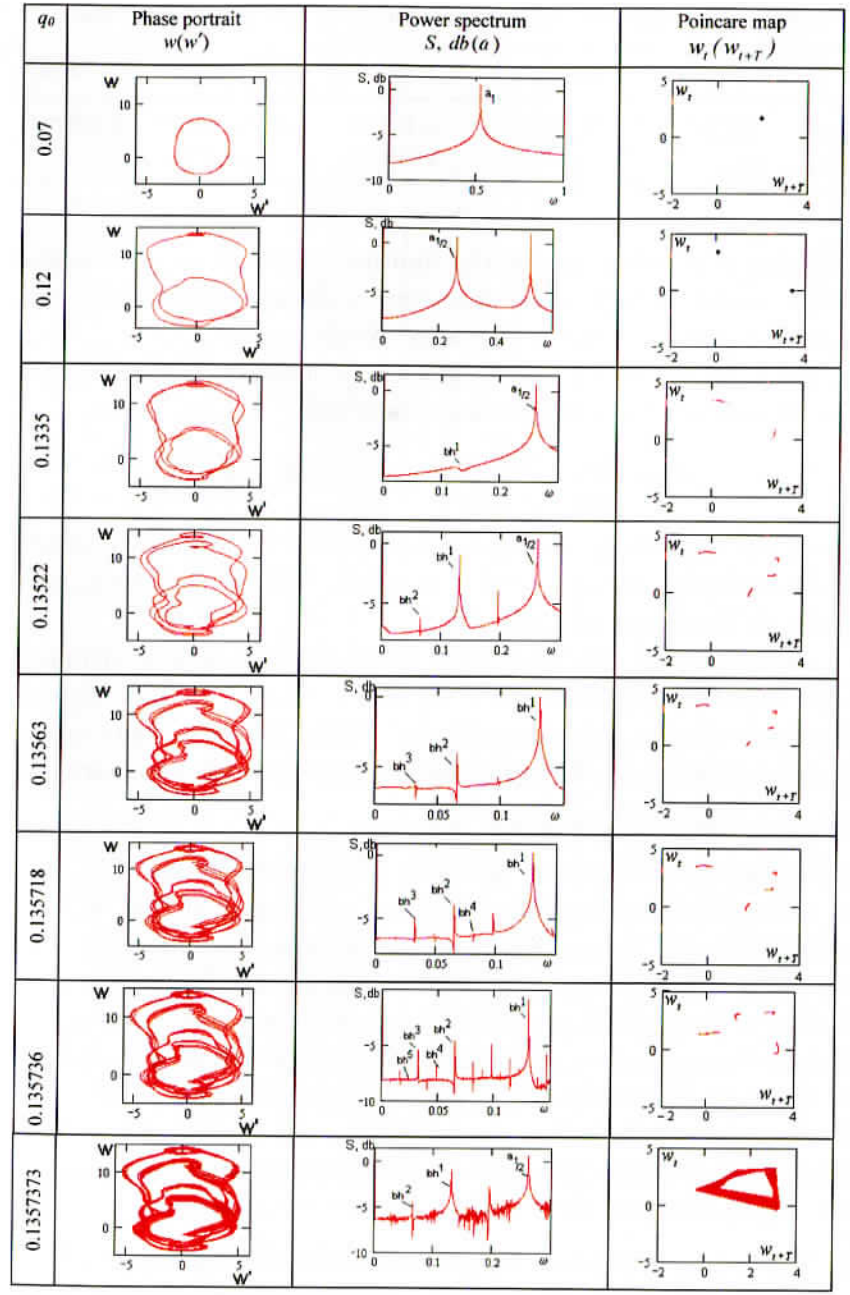

Fig. 9.27 Shell with simple moveable contour: phase portraits, power spectra and Poincaré maps for different q_0.

Table 9.7 Period doubling bifurcation of the axially symmetric shell.

n	1 bifurcation	2 bifurcation	3 bifurcation	4 bifurcation	5 bifurcation
$q_{0,\,n}$	0.1335	0.13522	0.13563	0.135718	0.1357369
d_n		4.19512	4.659091	4.656084	

following characteristics for the limiting values of q_0 are reported: phase portrait $w(w')$, power spectrum S, $db\,(\omega_p)$ and Poincaré maps $w_t\,(w_{t+T})$, where T is the period of excitation.

Table 9.7 allows to get the following convergent series regarding the estimation of the Feigenbaum constant

$$d_n = \frac{q_{0,n} - q_{0,n-1}}{q_{0,n+1} - q_{0,n}} = 4.65608466, \quad n = 5,$$

where the theoretical value of $d = 4.66916224$. The difference between theoretical and numerical value is 0.28%. Values of series $q_{0,\,n}$ and series d_n are shown in Table 9.7.

As a result of the vibrational process of the axially symmetric shell with the simple moveable contour for $b = 4$, we have detected the Smale chaotic attractors [Smale (1962)]. The latter ones are also known as attractors of Feigenbaum's type or strange attractors (SA).

Ruelle–Takens–Newhouse scenario

For a spherical shell with a simply supported contour (Fig. 9.20), as well as with moving (Fig. 9.23) and stiff clamping (Fig. 9.24) the classical Ruelle–Takens–Newhouse scenario has been detected, which we study in more detail here. The fundamental characteristics: time history $w\,(0,t)$, phase portrait $w(\dot{w}\,)$, power spectrum S, $db\,(\omega_p)$ and Poincaré maps $w_t\,(w_{t+T})$ versus the limiting values of q_0 are collected in Fig. 9.28. The values of q_0 are referred to as limiting, since between two successive values of q_0 the qualitative picture of dynamical state remains unchanged. We consider this scenario using an example of the rigidly clamped shell contour.

1. Vibrations take place on the fundamental frequency a_1 of excitation and they are periodic. Phase portrait presents a one-rotational limit cycle ($q_0 = 0.68$).

Fig. 9.28 Dynamic characteristics of the shell exhibiting Ruelle–Takens–Newhouse scenario versus different q_0.

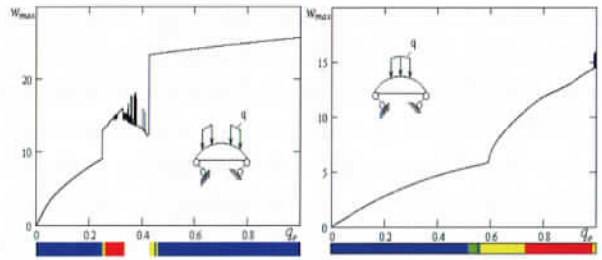

(a) (b)

Fig. 9.29 (a) Dependence $w_{\max}(q_0)$ of a shell with five and (b) four harmonically excited points.

remaining points $q = 0$; 2. The load $q = q_0 \sin(\omega_p t)$ is acting in five points $0 \le i \le 4$, where $0 \le i \le n$, $i, n \in N$ in a neighborhood of the center, and in remaining points $q = 0$.

Dependencies $w_{\max}(q_0)$ for the first and the second type loads are shown in Fig. 9.29(a) and 9.29(b), respectively. The first case is associated with two stiff bifurcations. The first stiff stability loss occurs while transiting from harmonic vibration to first Hopf bifurcation. The second stiff stability loss appears during transition from chaotic to harmonic vibrations, which is approved by the scale of signal types exhibiting period doubling bifurcations. In this case, the dependence $w_{\max}(q_0)$ is smoother, there is a first-order discontinuity as in the previous case. Scale of signal types exhibits a small zone of soft bifurcations and there is a lack of chaotic zones. Five period doubling bifurcations have been detected, and the numerically estimated Feigenbaum constant is 4.67784 ..., and its difference in comparison with the theoretical value is 0.168%.

For two types of local loads of the shell, the charts in the plane $\{q_0, \omega_p\}$ are reported (the first type is shown in Fig. 9.30(a), whereas the second has been presented in Fig. 9.30(b)). In the chart of the control parameter plane $\{q_0, \omega_p\}$ a large chaotic zone on the high frequencies is observed, whereas small zones of Hopf bifurcations are located on low frequencies (there are drops of independent frequencies and their linear combination).

Transition of the local load into the neighborhood of the shell center yields large zones of regular vibrations, whereas a small zone

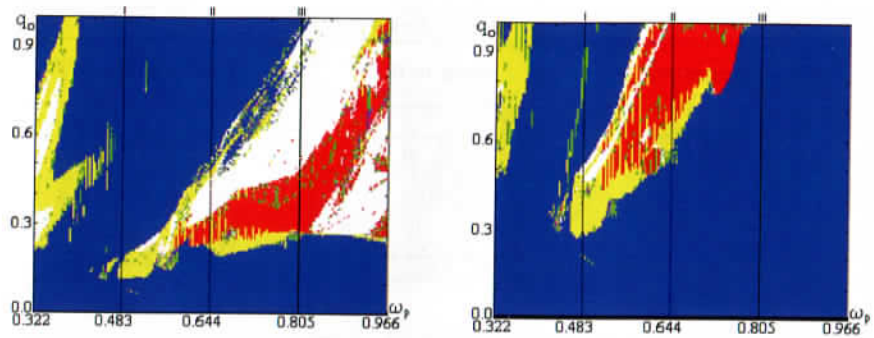

(a) (b)

Fig. 9.30 (a) Charts of shell vibrations on the control parameters $\{q_0, \omega_p\}$ plane with harmonic excitations in five and (b) four points.

of chaotic vibrations has been shifted into a space of low frequencies. In this case, drops of independent frequencies and their linear combinations do not exist.

9.2.5 *Sharkovsky's periodicity*

We investigate vibrations of the spherical axially-symmetric shell with simple movable support and the shallow parameter $b = 4$, with damping coefficient $\varepsilon = 0.1$, and subjected to harmonic load $q = q_0 \sin \omega_0 t$.

Within the chaotic region, windows of periodic vibrations following the Sharkovsky order have been detected. We study time histories/signals in the shell center, phase portraits, power spectra and Poincaré maps and we aim to trace the behavior of periodic orbits described in the Sharkovsky theorem. In Fig. 9.31, Sharkovsky order $2 \cdot 3$; $2 \cdot 5$ is exhibited. It should be mentioned that the so-called Sharkovsky's orders are not associated with each other, but they are rather detected separately in the whole plane $\{q_0, \omega_0\}$. The following dynamical features have been illustrated: in the Poincaré map a number of points is equal to the number of maxima in the power spectrum; order $2 \cdot 3$ — Poincaré map is divided into two subsets having 3 points each; order $2 \cdot 5$ — Poincaré map consists of 10 points, and the power spectrum exhibits 10 maxima. The phase portrait has loops,

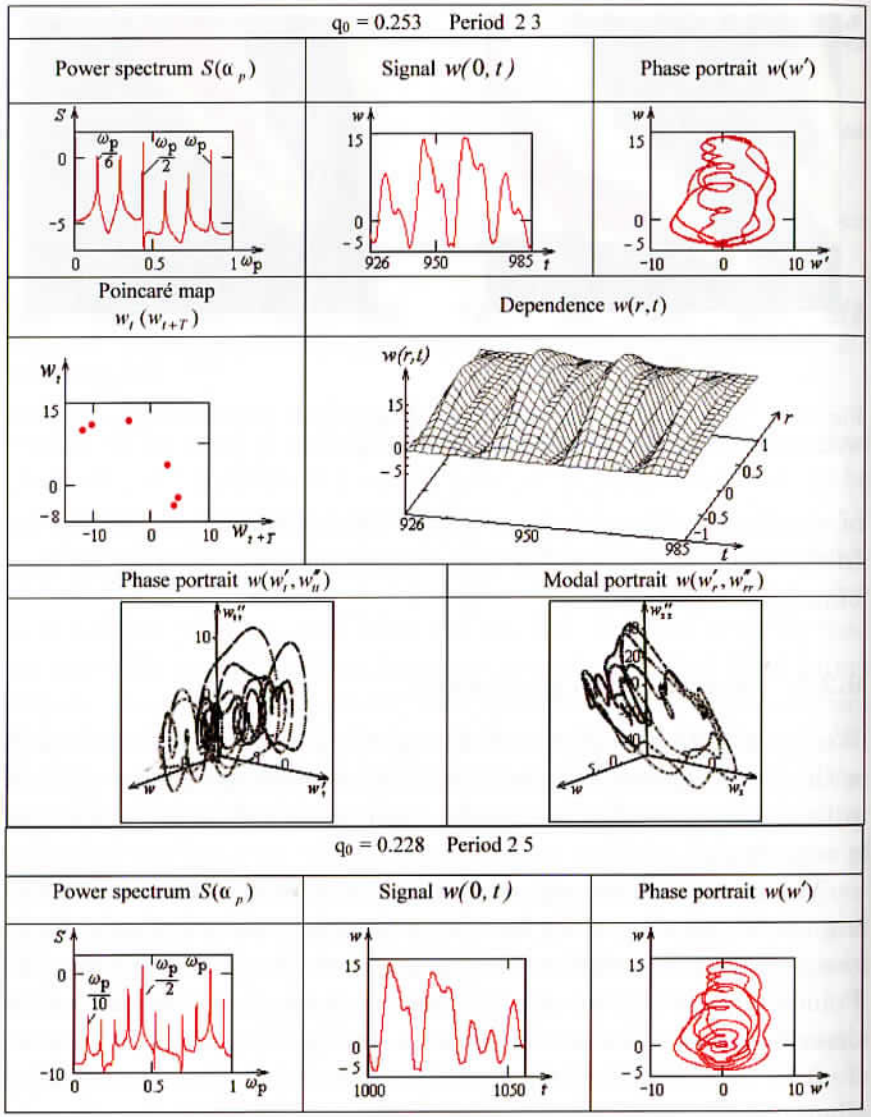

Fig. 9.31 Vibrations of shell with a simple movable support exhibiting Sharkovsky's orders of $2 \cdot 3$ and $2 \cdot 5$.

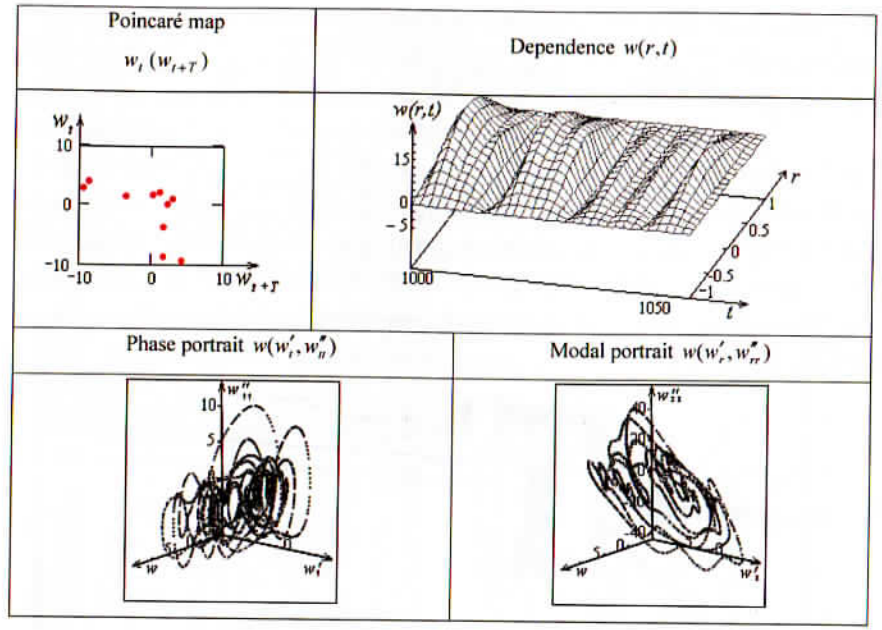

Fig. 9.31 (*Continued*)

and their number coincides with the number of points of the Poincaré map. Those orbits present periodic windows in chaos and their structure is the same in the whole analyzed set. The mentioned orbits can be also traced on the phase and modal portraits, constructed for three phase variables.

9.2.6 *Control of chaos*

We have carried out control of the circle shell loaded by the uniform periodic load $q = q_0 \sin(\omega_p t)$ by using two additional types of periodic excitations:

(1) Local transversal harmonic excitation is applied to five points $8 \le i \le 12$, where $0 \le i \le n$; $i, n \in Z$;
(2) Harmonic torque is applied.

Two types of excitations have been studied: fixed frequency and synchronization of frequencies. We study the system behavior, when the local harmonic load is applied. The system response has

Table 9.8 Applied surface and local shell loads.

Problem	Surface load	Local load
1.	$q = q_0 \cdot \sin(\omega_p \cdot t)$	—
2.	—	$q = q_0 \cdot \sin(\omega_p \cdot t)$
3.	$q = q_0 \cdot \sin(\omega_p \cdot t)$	$q_1 = 0.6\sin(0.6\,t)$
4.	$q = q_0 \cdot \sin(\omega_p \cdot t)$	$q_1 = 0.6\sin(0.725\,t)$
5.	$q = q_0 \cdot \sin(\omega_p \cdot t)$	$q_1 = 0.6\sin(0.886\,t)$

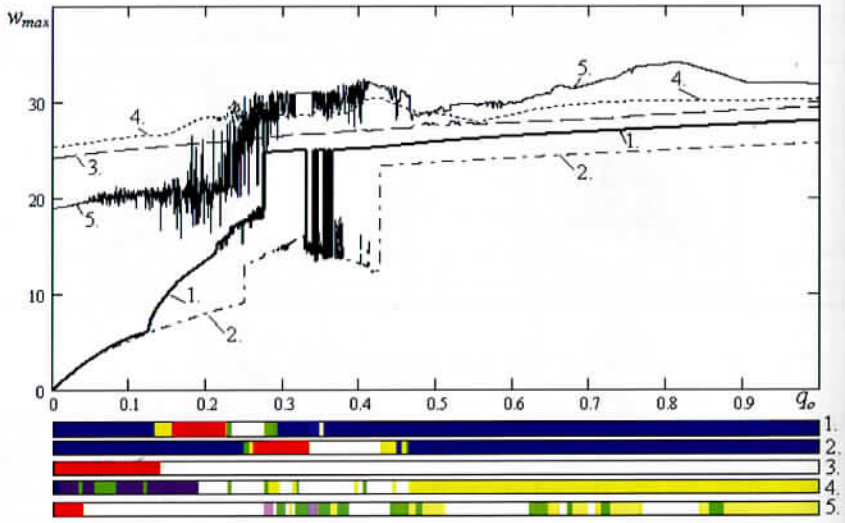

Fig. 9.32 Dependencies $w_{\max}(q_0)$ and vibrations character scales associated with five problems (see Table 9.8).

been monitored on the basis of numerical results and reported in a graphical form, where also the dependencies of the maximum shell deflection versus excitation amplitude as well as the charts of the vibration character versus control parameters have been shown using a color notation. Identification of the system vibration regime has been carried out with the help of the power spectrum analysis as well as the computation of Lyapunov exponents.

We consider the function $w_{\max}(q_0)$, when two types of the load act on the system: local and continuously distributed (Table 9.8). Five numbers of curves shown in Fig. 9.32 are identified by the corresponding number of problems given in Table 9.8.

Natural frequency of the shell is $\omega_0 = 0.644$. One may conclude that two-frequency excitation does not improve the vibration regime is seen in the figures (in the last three cases, the system works in harmonic regimes less than two first cases considered).

In order to investigate the shell behavior under the action of two exciting loads with different frequencies (problems 3–5 of Table 9.8), the mathematical model has been constructed and the charts of the vibrations character for the control parameters $\{q_0, \omega_p\}$ are reported in Fig. 9.33. All charts exhibit large zones of chaotic vibrations, while increasing the excitation frequency of the local load implies

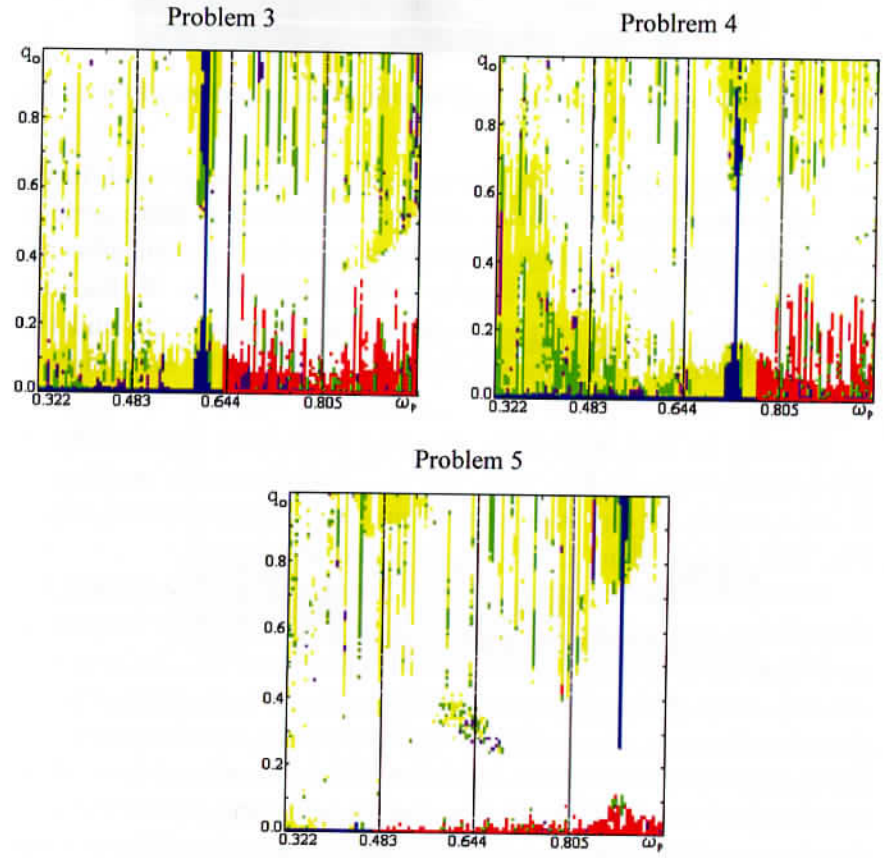

Fig. 9.33 Charts of vibration type versus control parameters $\{q_0, \omega_p\}$ and the associated number of solved problem.

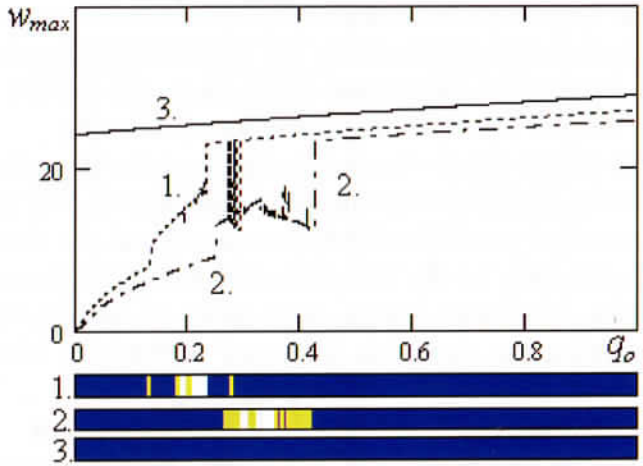

Fig. 9.34 Dependencies $w_{\max}(q_0)$ and the scales of solved problems for $\omega_p = 0.6$.

an increase in chaotic zones. As we have already mentioned, in the case of two-frequency excitation, the system is transited into periodic vibrations only if excitation frequencies are close to each other. In this case, on the charts of vibrations (Fig. 9.33) zones of chaos are located in the vicinity of the frequency of the local load, and this case has been more deeply studied with the help of dependencies $w_{\max}(q_0)$.

Namely, in Figs. 9.34–9.36, $w_{\max}(q_0)$ have been reported for all five loading cases. In Fig. 9.34, the $w_{\max}(q_0)$ curves for problems 1, 2, 3 ($\omega_p = 0.6$), in Fig. 9.35 for problems 1, 2, 4 ($\omega_p = 0.725$), and in Fig. 9.36 for problems 1, 2, 5 ($\omega_p = 0.886$) are shown.

In all cases, the coincidence of two frequencies of the external load decreases a zone of chaotic vibrations, both independent frequencies and bifurcation do not appear and the dependence $w_{\max}(q_0)$ becomes smooth. Area of chaotic zones and bifurcations and independent frequencies decrease, whereas a zone of periodic vibration increases (Fig. 9.35). We study the system behavior, when the second type of the exciting load is applied, i.e. the periodic load. In Fig. 9.37, the dependencies $w_{\max}(M_0)$ and $w_{\max}(q_0)$ as well as the scales characterizing the signal type for seven problems associated with the mentioned loading types are reported in Table 9.9.

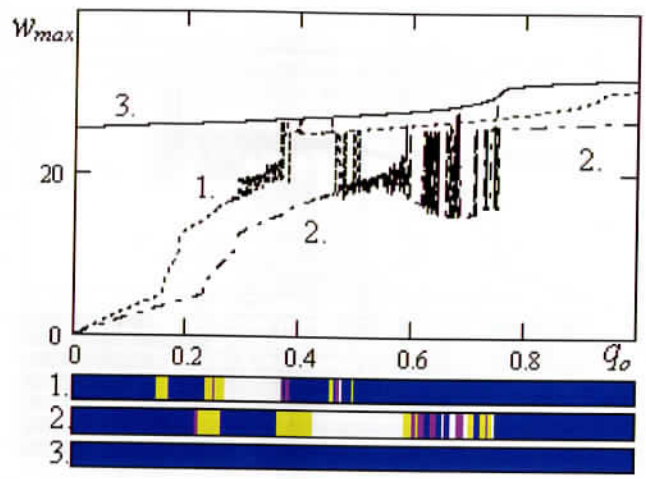

Fig. 9.35 Dependencies $w_{\max}(q_0)$ and the scales of solved problems for $\omega_p = 0.725$.

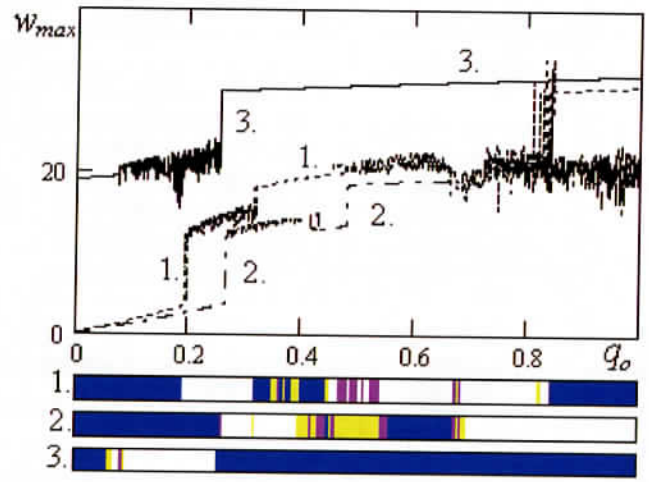

Fig. 9.36 Dependencies $w_{\max}(q_0)$ and vibration scales ($\omega_p = 0.886$).

The values of ω_p and M_0 have been chosen to illustrate the shell behavior in cases: the first point is taken on the boundary between chaos and bifurcations; the second is taken in deep chaos regime; the third is taken on the border of chaos and periodic vibrations, and the last in a zone of periodic vibrations. Let us analyze the case of

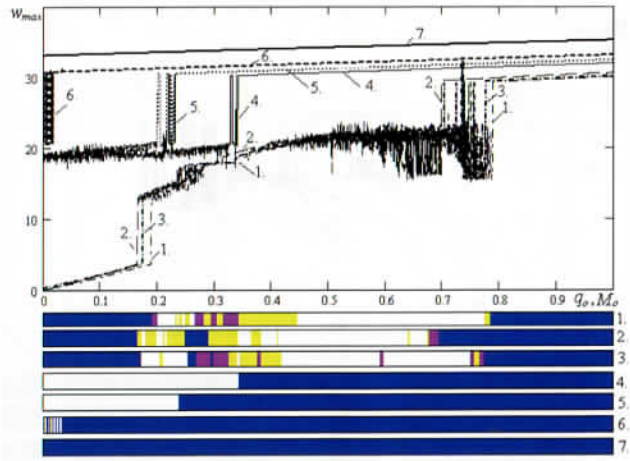

Fig. 9.37 Dependencies $w_{\max}(M_0)$ and $w_{\max}(q_0)$ and vibration scales.

Table 9.9 Shell loading types.

No	Continuous load	Resistance torque
1.	$q = q_0 \cdot \sin(\omega_p \cdot t)$	—
2.	—	$M = M_0 \cdot \sin(\omega_p \cdot t)$
3.	$q = q_0 \cdot \sin(\omega_p \cdot t)$	$M_1 = 0.1 \cdot \sin(0.859 \cdot t)$
4.	$q = q_0 \cdot \sin(\omega_p \cdot t)$	$M_1 = 3.4 \cdot \sin(0.859 \cdot t)$
5.	$q = q_0 \cdot \sin(\omega_p \cdot t)$	$M_1 = 4.2 \cdot \sin(0.859 \cdot t)$
6.	$q = q_0 \cdot \sin(\omega_p \cdot t)$	$M_1 = 5.5 \cdot \sin(0.859 \cdot t)$
7.	$q = q_0 \cdot \sin(\omega_p \cdot t)$	$M_1 = 9.6 \cdot \sin(0.859 \cdot t)$

chaotic zones (in Fig. 9.38, the following characteristics are shown: signal $w(0,t)$, where $1000 \le t \le 1100$, phase portrait $w(w')$, power spectrum $S(\omega_p)$, Poincaré map $w_t(w_{t+T})$).

In the beginning, we consider the shell dynamics in regimes where the shell is subjected to action of only one component of excitation, i.e. either the continuous periodic load or the periodic torque. Frequency of exciting load is the same in all cases ($\omega_1 = 0.859$). When the shell is subjected to action of the continuous load, a transition from periodic to chaotic vibration is carried out via a stiff stability loss. The analyzed power spectrum (in a chaotic zone) exhibits the local maximum on frequency $\omega_1/2$, in spite of the global maximum

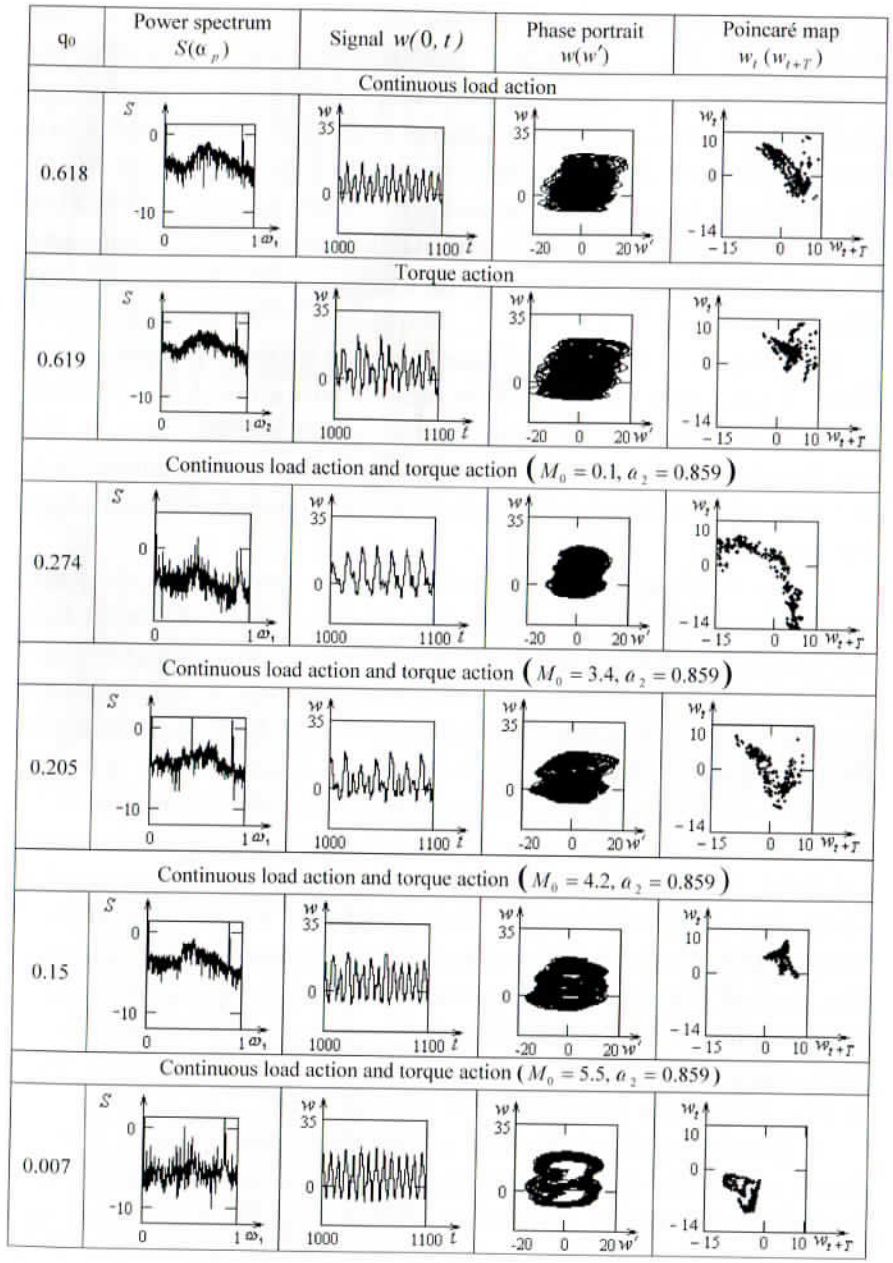

Fig. 9.38 Power spectrum, time histories/signals, phase portraits and Poincaré maps of the shell subjected to continuous load and torque actions.

on frequency ω_1. In order to control chaos, two exciting forces have been applied. We consider the case when the exciting torque has amplitudes $M_0 = 0.1; 3.4; 4.2$ and the frequency coincides with the frequency of the harmonic continuous load. Since the type of vibrations for all these cases is similar, we consider the influence of M_0 for the mentioned three cases simultaneously. The Poincaré map exhibits one attractor, whereas the phase portrait presents a continuous spot. We consider the influence of both exciting load and torque with $M_0 = 5.5$.

In this case, in the chaotic zone there are drops of periodic vibrations. A transition from chaotic to periodic vibrations takes place via the stiff stability loss. Contrary to the earlier studied zone, in this case the chaotic vibrations are changed: phase portrait represents an attractor of the shape of eight, whereas the Poincaré map consists of two attractors.

In the latter case, the excitation torque frequency $\omega_p = 0.859$, whereas its amplitude changes in the interval of $(0.1; 9.6)$. In all cases reported in Fig. 9.37, besides the cases of the periodic load and torque ($q_0 = 9.6$, $\omega_p = 0.859$), the maximum shell deflection curve exhibits the first-order discontinuity implying the stiff stability loss. Its occurrence is approved by the vibration character scales, since this time instant is associated with a change of the vibration character.

In order to study changes in the system's reaction on the external load, the charts of vibration types in the control parameters plane $\{q_o, \omega_p\}$ (problem 3–7, Table 9.9) and Fig. 9.39 have been constructed. Analysis of the obtained results implies that action on the shell of the continuous periodic load and the periodic torque with amplitude $M_0 = 0.1$ with the same frequency of both excitations, the detected chaotic zones are similar to those already shown in Fig. 9.40(b) for the case of the periodic load.

It means that the action of additional periodic torque with its small amplitude does not change essentially the shell vibrations. Increasing M_0 implies non-unique change in the chaotic region with respect to the global chart surface. Namely, in the beginning it starts to increase monotonously and it practically covers the whole chart area, then chaotic zone starts to decrease simultaneously shifting

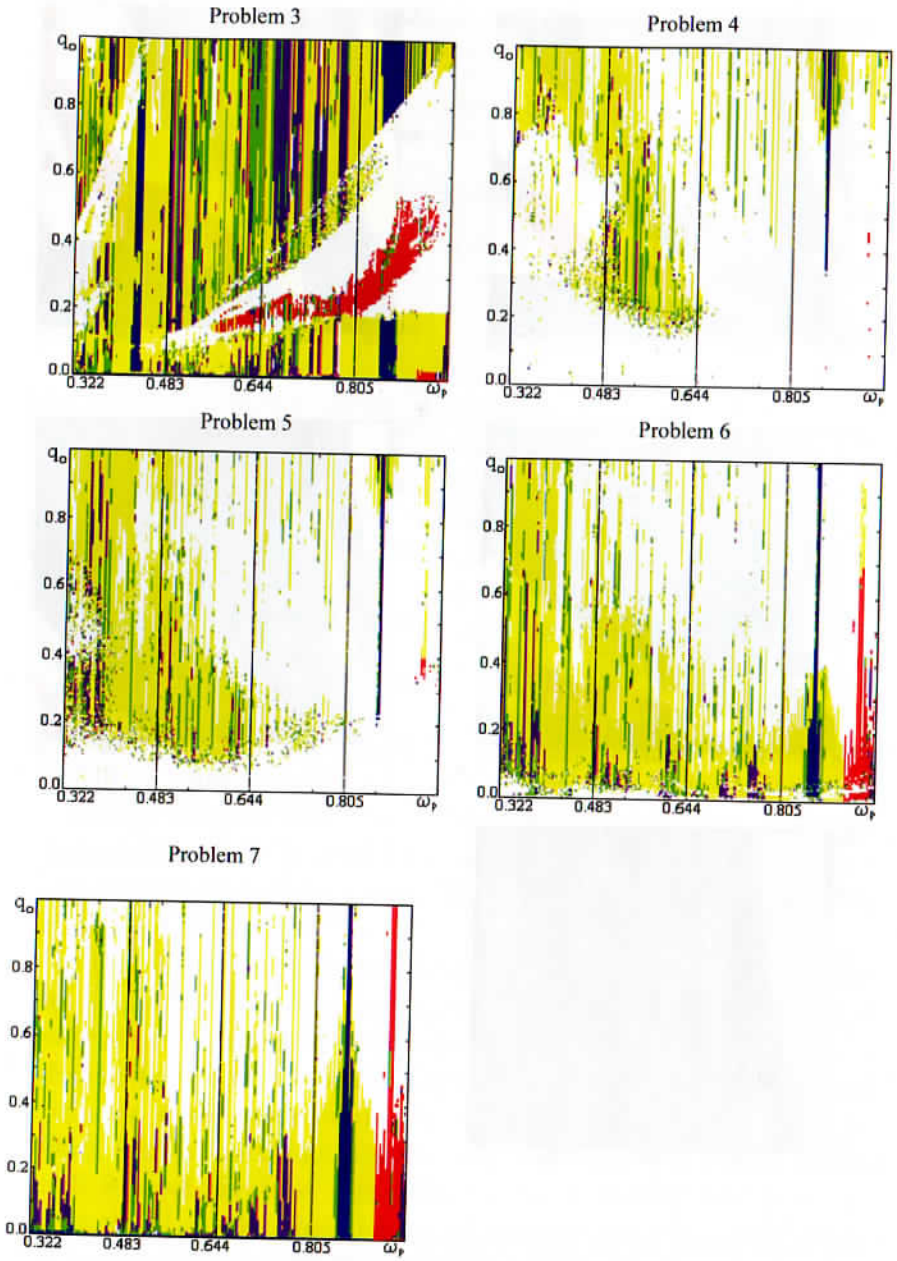

Fig. 9.39 Charts of vibration types of the shell subjected to continous load and resistance torque (problems 3–7, Table 9.9).

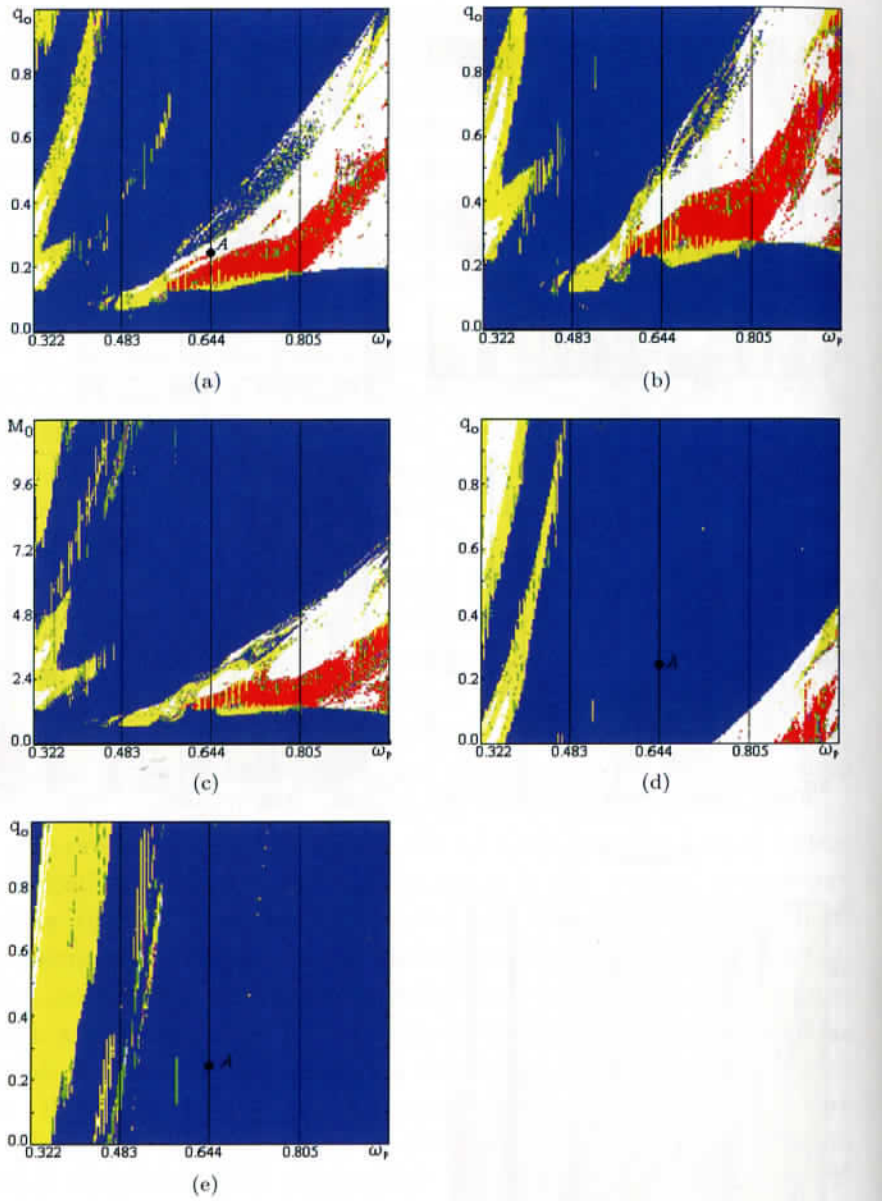

(a) (b) (c) (d) (e)

Fig. 9.40 Charts of the shell vibration types versus the control parameters $\{M_0, \omega_p\}$, $\{q_0, \omega_p\}$: (a) distributed load $q = q_0 \sin(\omega_p t)$, (b) local load $q_1 = q_0 \sin(\omega_p t)$, (c) support moment $M = M_0 \sin(\omega_p t)$, (d) distributed load $q = q_0 \sin(\omega_p t)$ and local load $q_1 = 0.6 \sin(\omega_p t)$, (e) distributed load $q = q_0 \sin(\omega_p t)$ and support moment $M_1 = 9.6 \sin(\omega_p t)$.

Table 9.10 Controlling vibrations of the shell using the continuous harmonic local force and the harmonic torque.

No	Continuous load	Local load	Torque
1.	$q = q_0 \sin(\omega_p t)$	—	—
2.	—	$q = q_0 \sin(\omega_p \cdot t)$	—
3.	—	—	$M = M_0 \sin(\omega_p t)$
4.	$q = q_0 \sin(\omega_p t)$	$q_1 = 0.6 \sin(\omega_p t)$	—
5.	$q = q_0 \sin(\omega_p t)$	—	$M_1 = 9.6 \sin(\omega_p t)$

into an area of higher values of q_0. Areas of periodic zones appear only if the frequencies are rational, then the chart exhibits a large area of bifurcations. Otherwise, an area of independent frequencies and their linear combinations appear. The increase in the excitation amplitude ($\omega_p = 0.859$) implies the increase in the periodic zone while the parameter q_0 is increased.

Analysis of the charts of control parameters for the first type of problems (3–5, Table 9.8) and the second type of problems (3–7, Table 9.9) allows to conclude that in the case of similar frequency $\omega_p = 0.859$ of the load and the torque, there exists a vertical zone, $\forall q_0 \in [0, 1]$, corresponding to periodic vibrations. This motivated us to consider the problems when the shell is subjected to uniformly distributed periodic load and the local load or the periodic torque while keeping the synchronized changes if the frequencies of both excitations (Table 9.10).

In Fig. 9.40, charts of the vibration types for the control parameters $\{q_0, \omega_p\}$, $\{M_0, \omega_p\}$ are reported. Analysis of the obtained results allows to conclude that the synchronization of external loads shifts the system to qualitatively different type of vibrations. Almost all chaotic zones occurring in the charts $\{q_0, \omega_p\}$, $\{M_0, \omega_p\}$ [Figs. 9.40(a), 9.40(b) and 9.40(c)] have been cancelled. In the case of the fourth type of the load [Fig. 9.40(d)] the vibrations are periodic. Only a small chaotic zone has been preserved as well as bifurcation on low and high frequencies. In the case of the fifth type of loading [Fig. 9.40(e)] there exist zones of bifurcations as well as small zones of chaos, but only on low frequencies.

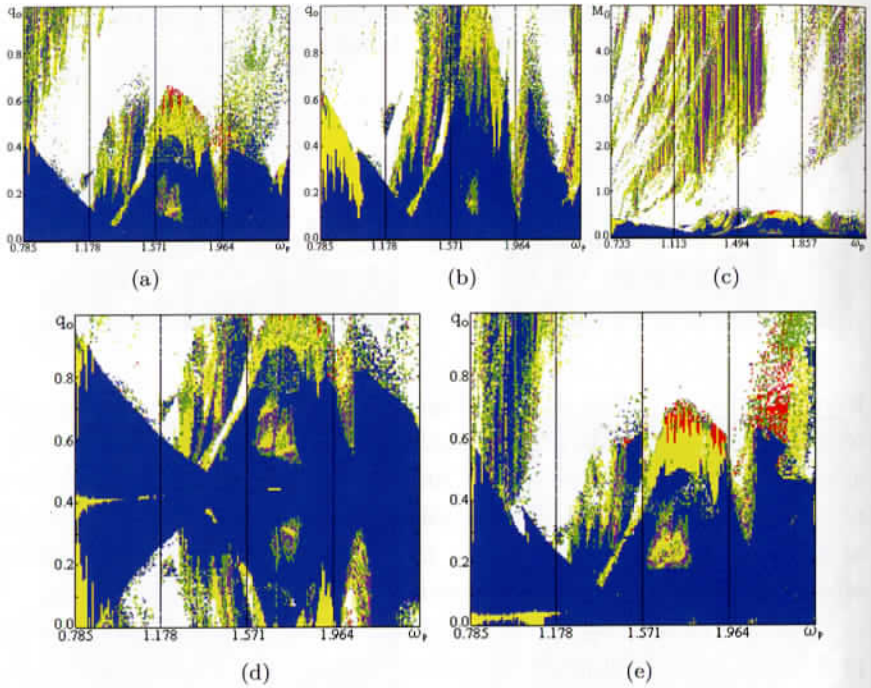

Fig. 9.41 Charts of vibration types $\{q_0, \omega_p\}$, $\{M_0, \omega_p\}$.

Similar investigations have been carried out for the shell with its contour and the shallow parameter $b = 4$. Results of the given investigations are shown in Fig. 9.41. Taking into account the earlier obtained results, our further analysis has not been carried out so deeply as it was done for the case of the shell with its simple moveable contour.

We have investigated the methods of chaos control, which have earlier given positive results and they have been applied to the shell with the simply supported contour. As in the previous case, we have constructed the charts of the control parameters for the case of uniformly distributed periodic load [Fig. 9.41(a)], and for the case of periodic torque [Fig. 9.41(b)] which have been also reported earlier. In addition, charts describing shell behavior subjected to periodic continuous and local load and torque actions have been given. All applied loads have been shown in Table 9.11 (observe that the phase

Table 9.11 Controlling vibrations of the shell using the continuous harmonic local force and the harmonic torque.

Problem	Continuous load	Local load	Torque
1.	$q = q_0 \sin(\omega_p t)$	—	—
2.	—	$q = q_0 \sin(\omega_p t)$	—
3.	—	—	$M = M_0 \sin(\omega_p t)$
4.	$q = q_0 \sin(\omega_p t)$	$q_1 = \sin(\omega_p t - \pi)$	—
5.	$q = q_0 \sin(\omega_p t)$	—	$M_1 = 0.5 \sin(\omega_p t)$

shift of the local load on the magnitude of π means that the local load works in the anti-phase with respect to the continuous load). Action of two additional loads yields a benefit, since after their introduction a decrease in chaotic zones and an increase in periodic zones take place. Influence of the additional local load is more effective with respect to energy dissipation as well as from the point of view of chaos control. The most important observation is that the methods of control of chaotic vibrations are the same for simple support, moveable and non-moveable support.

9.2.7 *Wavelet based analysis*

It has been shown earlier that a transition from periodic to chaotic vibrations of our mechanical system has been realized via the Feigenbaum scenario [Feigenbaum (1978)]. The latter scenario can be validated by numerical experiments of simple mathematical models. We have studied the shell with a simply supported moving resistance contour and the shell parameter $b = 4$. The Feigenbaum constant has been estimated for the control parameter q_0, where the bifurcations take place. The obtained numerical value

$$\alpha_n = \frac{q_{0,n} - q_{0,n-1}}{q_{0,n+1} - q_{0,n}} = 4.65608466, \qquad n = 5$$

well coincides with its theoretical counterpart $\alpha = 4.66916224$ [Schimmels and Palaiotto (1994)], and the difference is of 0.28%.

In order to study bifurcational and chaotic vibrations of the flexible axially symmetric shallow shells the wavelet transforms on the basis of Gauss wavelets of order from $m = 1$ to $m = 8$ as well as

real and complex Morlet wavelets have been applied. For further research, we have chosen the Morlet and Gauss of $m = 1$ and $m = 8$ wavelets as the most representative and reliable. In order to estimate the Feigenbaum constant α, we have used the one-dimensional (1D) Fourier transform, yielding also a 1D information on the relative input (amplitude) of various time scales (frequencies). Contrary to the 1D Fourier transform, the wavelet transform on 1D series yields 2D set of coefficients of the wavelet transform $W(t, \omega)$. Distribution of these coefficients values in the space (t, ω) (time scales, frequency localization) gives information of the evolution of relative input of different scales in time, and it is called a spectrum of coefficients of wavelet transform or equivalently a wavelet spectrum.

In Figs. 9.42(a)–9.43(c) and 9.44 (a, b) for different values of the parameter q_0, the wavelet spectra of 1D signal (i.e. magnitudes of $|W(t,\ \omega)|$) as well as surfaces in a 3D space and their projections on the surface $(t,\ \omega)$ in the form of 2D and 3D wavelets, Poincaré maps, power spectra and phase portraits are given.

The charts reported in Figs 9.42–9.44 allow to follow the change of amplitudes of wavelet transformation regarding various scales and in time, as well as pictures of curves of local extrema on those surfaces (the so-called skeleton diagrams). In Figs. 9.42–9.44, the abscissa axis denotes time, whereas the ordinate axis presents the time scale. Light chart regions correspond to large, whereas dark regions correspond to small values of the energy density $|W(t,\ \omega)|$. Grey color of charts (Figs. 9.42–9.44) exhibits regions of wavelet transform values for small time intervals, which are gathered in the second column of each of the reported Figs. 9.42 and 9.43 in the enlarged window scale. In the case of the complex Morlet wavelet (Fig. 9.44) such a window denotes the time interval, for which in the second column a surface of arguments corresponding to the coefficients of the wavelet-transformation, is shown (the latter coefficients are complex numbers).

Analysis of chaotic vibrations of flexible axially symmetric shallow shells under action of the transversal periodic load with the help of the wavelets Gauss 1 and Gauss 8 yields approximated qualitative results, and does not describe the whole complex picture of

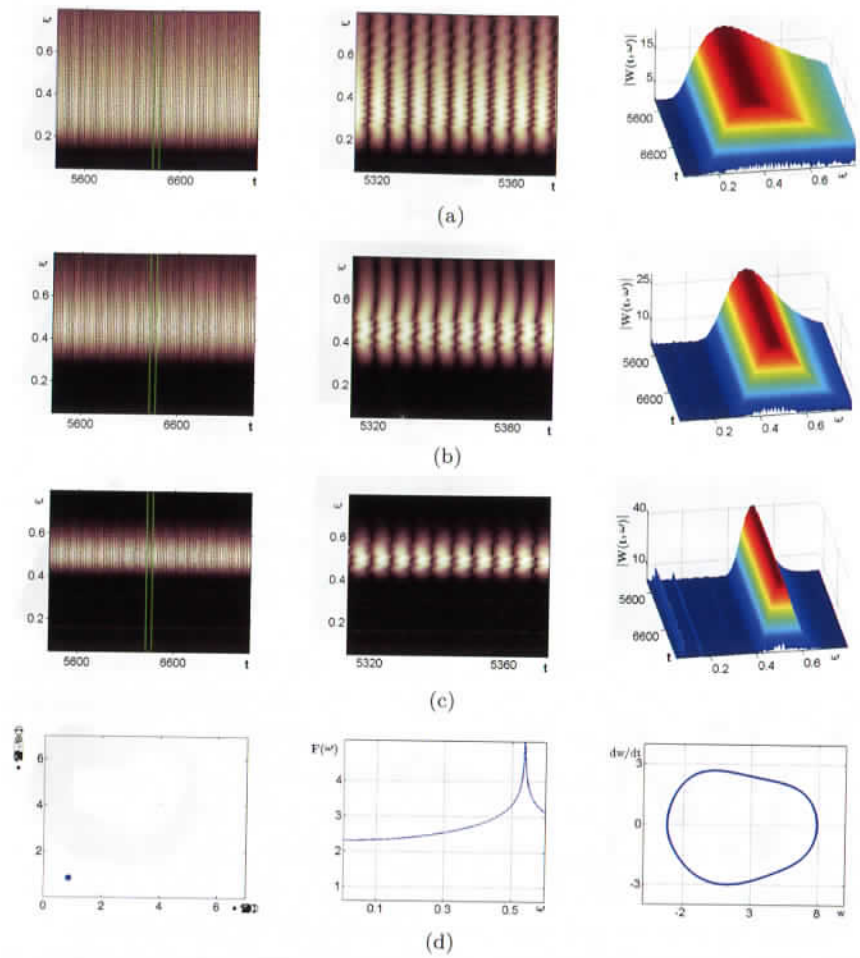

Fig. 9.42 row (a) Shell's periodic vibrations: 2D wavelet spectrum (Gauss 1), its enlarged window, and 3D wavelet spectrum (Gauss 1); row (b) 2D wavelet spectrum (Gauss 8), its enlarged window, and 3D wavelet spectrum (Gauss 8); row (c) 2D wavelet spectrum (Morlet), its enlarged window, and 3D wavelet spectrum (Morlet); row (d) Poincaré map, frequency power spectrum and phase portrait.

vibrations. The validated description of chaotic vibrations may yield only Morlet wavelets both real and complex. Our experience shows that in the case of the studied shallow rotational shells the most suitable for a reliable study are the complex Morlet wavelets. They

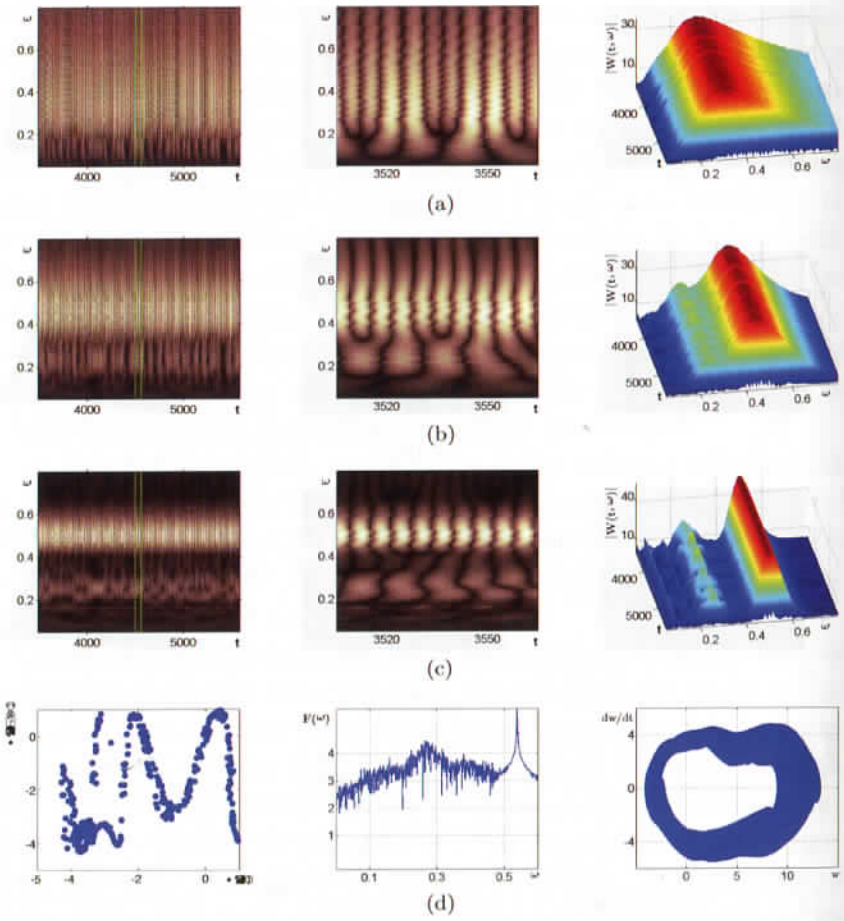

Fig. 9.43 row (a) Shell's chaotic vibrations: 2D wavelet spectrum (Gauss 1), its enlarged window, and 3D wavelet spectrum (Gauss 1); row (b) 2D wavelet spectrum (Gauss 8), its enlarged window, and 3D wavelet spectrum (Gauss 8); row (c) 2D wavelet spectrum (Morlet), its enlarged window, and 3D wavelet spectrum (Morlet); row (d) Poincaré map, frequency power spectrum and phase portrait.

possess good properties of the real Morlet wavelet, i.e. good frequency localization from one side, whereas from the other side the values of arguments of the corresponding wavelet-coefficients yield additional information allowing to visualize the properties of self-similarity on different scales monitored in a chaotic signal (see Fig. 9.44(b) for

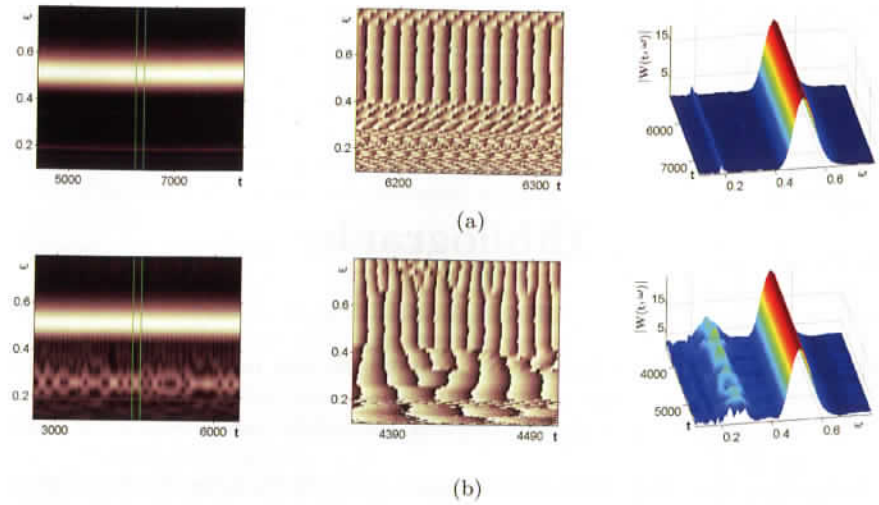

Fig. 9.44 Chaotic vibrations of the shell using different scales (rows (a), (b) for $q_0 = 0.14$: 2D wavelet spectrum (complex Morlet), its enlarged window, and 3D wavelet spectrum (complex Morlet).

$q_0 = 0.14$). The mentioned benefit of the Morlet wavelet allows to win with other wavelets. A Morlet wavelet has the largest number of zero moments compared with other wavelets, which allows for reliable and validated description of chaotic vibrations of the flexible shallow shells. The complex Morlet wavelet can be also applied in those cases when we aim at observing possible violations of the uncertainty principle. It seems that the study shows that a choice of the wavelet type depends on the vibration regime, and has its own peculiarity. Though in quantum mechanics the Pauli wavelets have been mainly applied, it seems that the complex Morlet wavelet is most suitable for the problems of theory of flexible structural members including shells.